Bioactive Materials 49 (2025) 399–417

Contents lists available at ScienceDirect

Bioactive Materials

journal homepage: www.keaipublishing.com/en/journals/bioactive-materials

Regulating macrophage glucose metabolism homeostasis via mitochondrial rheostats by short fiber-microsphere scaffolds for bone repair

Pengzhen Zhuang [a,b,c], Yu Chen [a,b,c], Yu Zhang [a,b,c], Wu Yang [a,b,c], Guilai Zuo [b], Jessica M. Rosenholm [c,d], Zhongmin Wang [a], Juan Wang [b,*], Wenguo Cui [b,**], Hongbo Zhang [a,c,d,***]

[a] Department of Radiology, Ruijin Hospital Lu Wan Branch, Shanghai Jiaotong University School of Medicine, Shanghai, 200025, PR China
[b] Department of Orthopaedics, Shanghai Key Laboratory for Prevention and Treatment of Bone and Joint Diseases, Shanghai Institute of Traumatology and Orthopaedics, Ruijin Hospital, Shanghai Jiao Tong University School of Medicine, 197 Ruijin 2nd Road, Shanghai 200025, P. R. China
[c] Pharmaceutical Sciences Laboratory, Faculty of Science and Engineering, Åbo Akademi University, Turku, 20520, Finland
[d] Turku Bioscience Centre, University of Turku and Åbo Akademi University, Turku, 20520, Finland

ARTICLE INFO

Keywords:
Glucose metabolism
Mitochondrial metabolic homeostasis
Mitochondrial rheostat
Short fibers
Hydrogel microspheres

ABSTRACT

The alterations in glucose metabolism flux induced by mitochondrial function changes are crucial for regulating bone immune homeostasis. The restoration of mitochondrial homeostasis, serving as a pivotal rheostat for balancing glucose metabolism in immune cells, can effectively mitigate inflammation and initiate osteogenesis. Herein, an ion-activated mitochondrial rheostat fiber-microsphere polymerization system (FM@CeZnHA) was innovatively constructed. Physical-chemical and molecular biological methods confirmed that CeZnHA, characterized by a rapid degradation rate, releases Ce/Zn ions that restore mitochondrial metabolic homeostasis and M1/M2 balance of macrophages through swift redox reactions. This process reduces the glycolysis level of macrophages by down-regulating the NF-κB p65 signaling pathway, enhances their mitochondrial metabolic dependence, alleviates excessive early inflammatory responses, and promptly initiates osteogenesis. The FM network provided a stable platform for macrophage glycolytic transformation and simulated extracellular matrix microenvironment, continuously restoring mitochondrial homeostasis and accelerating ossification center formation through the release of metal ions from the internal CeZnHA for efficient bone immune cascade reactions. This strategy of bone immunity mediated by the restoration of macrophage mitochondrial metabolic function and glucose metabolic flux homeostasis opens up a new approach to treating bone defects.

1. Introduction

Glucose metabolism is an important event in the control of macrophage-mediated inflammatory responses, and how glucose is utilized determines the fate of macrophages in immune regulation [1]. As key components of the human immune system, macrophages sense injury signals, and are activated into a pro-inflammatory phenotype, and secrete pro-inflammatory factors and chemokines to combat infections, amplify inflammatory responses, recruit immune cells, and attract cells associated with regeneration [2]. However, the inflammatory storm induced by uncontrolled inflammatory macrophages under pathological conditions leads to a loss of the body's inherent immune homeostasis, continues to amplify the inflammatory response, and ultimately results in tissue repair failure. Therefore, ensuring the time-sequential transition and gradient balance of macrophages from a pro-inflammatory phenotype to an anti-inflammatory phenotype is crucial for maintaining the immune microenvironment at the site of injury. Studies have shown that changes in glycolysis and oxidative phosphorylation serve as signals in macrophages to regulate immunomodulatory functions, characterized by macrophages transforming into a pro-inflammatory

Peer review under the responsibility of KeAi Communications Co., Ltd.
* Corresponding author.
** Corresponding author.
*** Corresponding author. Department of Radiology, Ruijin Hospital Lu Wan Branch, Shanghai Jiaotong University School of Medicine, Shanghai 200025, PR China.
E-mail addresses: juanwang1006@126.com (J. Wang), wgcui@sjtu.edu.cn (W. Cui), hongbo.zhang@abo.fi (H. Zhang).

https://doi.org/10.1016/j.bioactmat.2025.03.008
Received 27 October 2024; Received in revised form 6 March 2025; Accepted 7 March 2025
Available online 15 March 2025

phenotype (M1) through enhanced glucose uptake and glycolytic and into an anti-inflammatory phenotype (M2) through strengthened fatty acid oxidation and oxidative phosphorylation processes [3,4]. Therefore, regulating glucose metabolism homeostasis in macrophages at the injured site to maintain an appropriate pro-inflammatory/anti-inflammatory gradient is essential for tissue repair.

Mitochondria are key organelles that regulate glucose metabolism in cells [5]. The hypoxic environment of the damaged tissue leads to the increase of the level of cellular glycolysis, thus aggravating the disease process [6,7]. However, effective activation of macrophages in injured tissues depends on the coordinated regulation of glycolysis and mitochondrial metabolism [8,9]. On the one hand, in the early stages of acute injury, macrophages primarily rely on glycolysis rather than oxidative phosphorylation to rapidly supply energy and support anabolism [10,11]. Glycolysis produces energy at a rate 100-fold higher than oxidative phosphorylation, and biosynthetic intermediates (e.g., nucleotides) produced through the rapid initiation of glycolysis support the secretion of various pro-inflammatory cytokines by inflammatory macrophages, including tumor necrosis factor alpha (TNF-α), monocyte chemotactic protein-1 (MCP-1), interleukin 1 (IL-1), and interleukin 6 (IL-6), enhancing macrophage adaptation to the injured microenvironment [12,13]. Although the process of glycolysis occurs in the cellular matrix, it is dependent on mitochondrial function. Elevated glycolysis rates and constant oxygen depletion in the local environment lead to a higher NADH/NAD + ratio during cellular proliferation, consequently causing redox imbalance and increasing reactive oxygen species (ROS) production [14–17]. On the other hand, a significant portion of glycolytic pyruvate is translocated to the mitochondria for oxidation and ATP production, stabilizing HIF-1α expression through the generation of ROS. This promotes neovascularization at the wound site, providing oxygen and nutrients for tissue healing, indicating that the effective activation of early M1 macrophages is crucial for initiating tissue healing [18,19]. Kuninaka's analysis of marker genes for anti-inflammatory and pro-inflammatory macrophage phenotypes in wounds showed that the inflammatory macrophage population peaked at 1–3 days, and by 3–6 days, anti-inflammatory macrophages began to dominate wound healing [20]. During the tissue remodeling phase, macrophages rely on oxidative phosphorylation and the mitochondria's excitotoxic effects to enhance adaptability, prolong their survival in tissues, and thereby exert long-term tissue remodeling functions. Meanwhile, M2 macrophages produce various anti-inflammatory mediators involved in tissue remodeling and repair, including interleukin 10 (IL-10), transforming growth factor beta (TGF-β) and chitinase 3-like 3 (YM1) [21,22]. Therefore, regulating mitochondrial metabolic homeostasis is critical to ensuring the balance between glycolytic and oxidative phosphorylation processes in macrophages at various stages of injured tissue.

Mitochondria, as key rheostats of innate immunity and skeletal homeostasis, influence immune responses by regulating the metabolic state of immune cells, particularly macrophages. Their functional state directly affects the normal progression of innate immunity and skeletal homeostasis. Gu et al. reported that a liver cytomimetic scaffold could retrogradely translocate arginase 2 (Arg2) from mitochondria to the cytoplasm, reprogramming the mitochondrial tricarboxylic acid cycle, oxidative phosphorylation, and arginine metabolism, thereby remodeling bone immune homeostasis [23]. He et al. demonstrated that molybdenum-doped bioceramic scaffolds actively participate in regulating bone immunohomeostasis in dental tissues and facilitate the transition of macrophages from glycolysis to mitochondrial oxidative phosphorylation [24]. In fact, an important feature of the transformation of inflammatory macrophages into anti-inflammatory macrophages and the differentiation of mesenchymal stem cells (MSCs) into osteoblasts in injured bone tissue is reduced glycolysis and enhanced oxidative phosphorylation. Among them, mitochondria-derived ROS play a crucial role in glycolysis-mediated macrophage activation, leading to an inflammatory macrophage phenotype by activating nuclear factor-κB (NF-κB) into the nucleus and inducing its phosphorylation [25–28]. Therefore, the removal of macrophage mitochondrial ROS during the tissue healing phase effectively inhibits NF-κB activation and coordinates mitochondrial metabolic alterations to restore normal glycolysis and oxidative phosphorylation levels, thereby reprogramming macrophages to an anti-inflammatory phenotype. Currently, a variety of bioactive materials are employed to scavenge ROS and modulate macrophage functional shifts, including organic molecules (e.g., N-acetyl-L-cysteine [29], α-tocopherol [30], superoxide dismutase mimics [31]) and inorganic nanomaterials (e.g., Ce-based nanomaterials [32], Mn-based nanomaterials [33], quantum dots [34]). However, the above materials exhibit poor degradation properties, low mitochondria targeting efficiency, high toxicity, and an inability to sustainably regulate mitochondrial homeostasis, which limits their further application. Therefore, developing a scaffold that matches the tissue immune gradient and continuously regulates mitochondrial functional homeostasis to ensure the time-sequential balance of mitochondrial oxidative phosphorylation and glycolysis in macrophages during the inflammatory and healing stages will better maintain innate immunity and skeletal homeostasis.

In this study, inspired by macrophage metabolic reprogramming characteristics and mitochondrial regulation strategies, mitochondrial rheostats fiber microsphere scaffolds that can restore macrophage mitochondrial function and glucose metabolism fluxes were innovatively constructed by guiding the polymerization of short fibers and hydrogel microspheres (Scheme 1). CeZnHA dynamically removed ROS from macrophage mitochondria through a REDOX process, thereby restoring functional homeostasis. The fiber network (FM) mimicked the extracellular matrix microenvironment of cancellous bone, providing cell growth space and mechanical support for the injury site. FM also provided a stable platform for regulating macrophage function, and the hydrogel microspheres inside it continuously release metal ions to restore the mitochondrial metabolism and M1/M2 balance of macrophages under oxidative stress, accelerating the formation of ossification centers and realizing highly efficient osteoimmunological cascade reactions. Firstly, the physicochemical properties of the mitochondrial varactors were investigated, and secondly, their ability to target macrophage mitochondria and scavenge ROS was verified, and the mechanism of regulating macrophage mitochondrial metabolism was explored. Next, the immune-osteogenic effects following the regulation of macrophage mitochondrial metabolism were evaluated. Finally, a rat femoral condylar defect model was constructed and implanted with mitochondrial rheostat scaffolds. Both the early immune response and the later osteogenic ability at the defect site were investigated. Mitochondrial rheostats, constructed from short fibers and microspheres, which restore mitochondrial function and regulate macrophage glucose metabolism, offer new strategies for repairing various tissue injuries.

2. Results and discussion

2.1. Design of mitochondrial rheostats

Mitochondrial rheostats consist of mitochondria-targeted microspheres with a rapid degradation rate and photo-crosslinked short fibers with a slower degradation rate. The core components include mitochondria-targeted Ce/Zn-doped hydroxyapatite (HA) nanoparticles, fast-degrading gelatin microspheres, and photoresponsive polylactic acid/gelatin methacryloyl (PLA/GelMA) short fiber scaffolds. Initially, Ce/Zn-doped HA nanoparticles were successfully synthesized according to a previously reported method. As an excellent bone repair material, HA has shown considerable value in nanocarriers, surface coatings, and bone grafts. To enable mitochondrial targeting by Ce/Zn-doped HA nanoparticles, triphenylphosphine was grafted onto amino-modified CeZnHA via an amide reaction, thereby creating a positive surface charge that facilitated binding to negatively charged mitochondria. However, large doses of nanomaterials are biotoxic, so the use

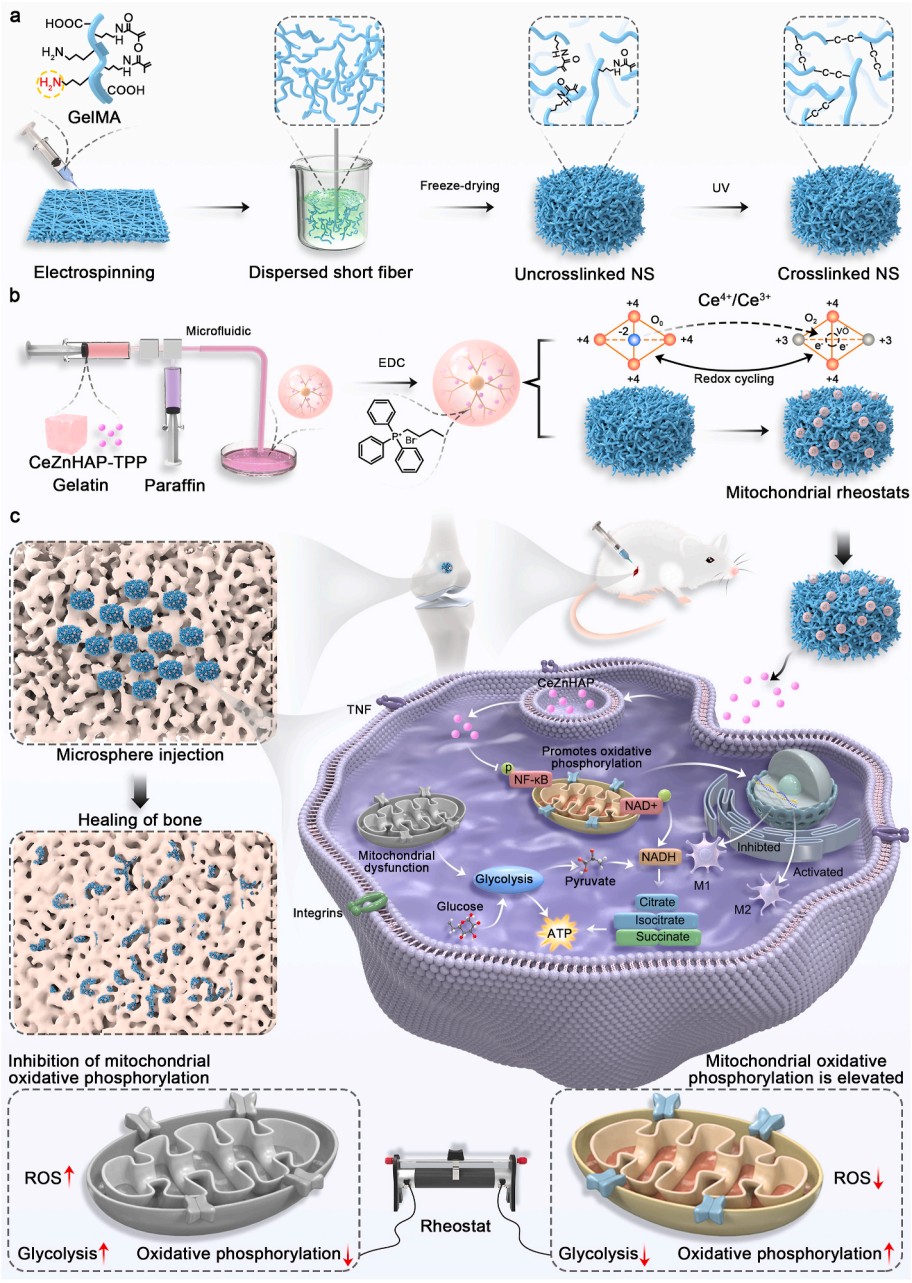

Scheme 1. Mitochondrial rheostat fiber scaffolds regulating macrophage glucose metabolism for bone repair treatment. a) Preparation of GelMA electrostatic spinning and subsequent homogenization to form short fibers. b) CeZnHAP microspheres were prepared using microfluidic technology and then composited with short fibers to form the mitochondrial rheostat fiber scaffolds. c) Schematic diagrams illustrating that mitochondrial rheostat fiber scaffolds restored macrophage mitochondrial metabolic function and glucose metabolic flux during the early-stage bone injury, effectively reducing the inflammatory storm and rapidly initiating the osteogenic process.

of gelatin microspheres to encapsulate nanomaterials is a suitable slow-release method to achieve their biological function in tissues. Additionally, 1-ethyl-3-(3-dimethylaminopropyl) carbodiimide hydrochloride (EDC) was used to crosslink gelatin microspheres loaded with CeZnHA, resulting in weakly crosslinked gelatin microspheres capable of rapidly and stably releasing CeZnHA for targeted mitochondria delivery. However, the weak cross-linking strength of the gelatin microspheres is not stationary within the tissue to build extracellular matrix-like structures and provide mechanical support. To address this, PLA/GelMA fiber membranes were prepared using electrospinning technology, which was then converted into a short fiber solution using a high-speed homogenizer. This solution was homogeneously mixed with CeZnHA-loaded gelatin microspheres and freeze-dried to form a stable fiber sponge structure. Finally, the fiber sponge scaffolds were infiltrated with a pre-cooled lithium phenyl (2,4,6-trimethylbenzoyl) phosphinate (LAP) solution and solidified by UV light initiation. This system provides a class of extracellular matrix-like structures that can provide mechanical support and a platform for the translation of biological functions to sites of early bone injury. Specifically, at the site of early bone injury, many macrophages gathered around the scaffold, and the gelatin microspheres inside the scaffold gradually released nanoparticles, which targeted macrophage mitochondria and scavenged ROS, accelerating the macrophage metabolism from glycolysis to oxidative phosphorylation process, and the increase in M2 macrophages accelerated the repair of bone defects.

2.2. Physicochemical characterization of mitochondrial rheostats

HA and Zn-doped HA nanoparticles were prepared by co-precipitation, and Ce/Zn-doped HA was subsequently obtained by inducing cerium nitrate deposition on the Zn-doped HA surface, using polyvinyl alcohol (PVA) as a templating agent and hexamethylenetetramine as the basic solution. Additionally, amino groups were introduced to Ce/Zn-doped HA using 3-aminopropyltriethoxysilane (APTES), and triphenylphosphine with carboxyl groups was grafted on its surface (CeZnHA) through an amide reaction (Fig. 1a). The morphology and elemental distribution of CeZnHA nanoparticles were characterized using scanning electron microscopy (SEM) and transmission electron microscopy (TEM). As shown in Fig. 1b and S1, CeZnHA nanoparticles consist of needle-like crystals with lengths and widths of 200 nm and 20 nm, respectively. Energy spectroscopy results show that the elements Ce, Zn, Ca, P and O are uniformly distributed on the nanoparticle surfaces, which indicates the successful doping of Ce and Zn. X-ray photoelectron spectroscopy (XPS) and x-ray diffractometer (XRD) were further

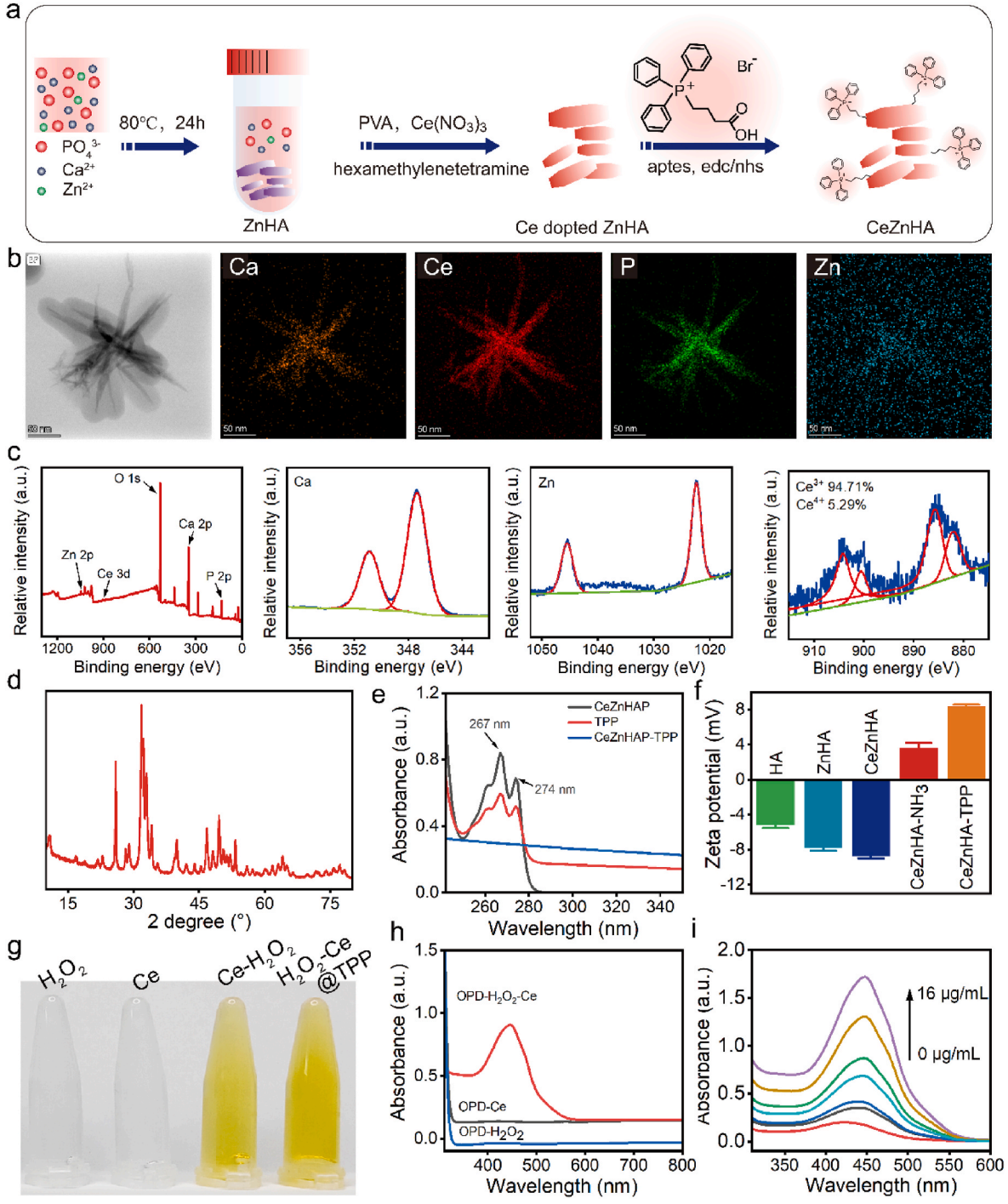

Fig. 1. a) Preparation and characterization of CeZnHAP nanoparticles. b) TEM images and elemental distributions, c) XPS patterns and d) XRD patterns of CeZnHAP nanoparticles. e) UV absorption spectra of CeZnHAP, TPP, and CeZnHAP-TPP. f) Zeta potentials of HAP, ZnHAP, CeZnHAP, CeZnHAP-NH_3, and CeZnHAP-TPP. g) Optical pictures and UV absorption spectra of Ce ion scavenging hydrogen peroxide. h, i) UV absorption spectra of ROS scavenging by different concentrations of CeZnHAP-TPP.

employed to analyze the elemental valence and physical phases of CeZnHA nanoparticles. The results depicted as in Fig. 1c show that the XPS spectra of CeZnHA nanoparticles contain Ce3d, Zn2p, Ca2p, P2p and O1s characteristic peaks, with trivalent and tetravalent Ce comprising 94.71 % and 5.29 %, respectively. The XRD patterns further proved that CeZnHA corresponds to hydroxyapatite, matching the PDF card number 09–0432 (Fig. 1d). As shown in Fig. 1e, the successful modification of triphenylphosphine was further confirmed by ultraviolet–visible (UV–vis) spectrophotometry, indicated by the presence of two characteristic peaks of triphenylphosphine (TPP) in the UV–vis spectra of CeZnHA at 267 nm and 274 nm, respectively. Zeta potential results showed negative charges on the surfaces of HA, ZnHA, and CeZnHA, while the amine-modified and TPP-grafted CeZnHA exhibited a charge of 8.36 ± 0.21 mV, implying that TPP-modified CeZnHAP nanoparticles can cross the cell membrane and bind to mitochondria (Fig. 1f). Notably, CeZnHA exhibits the ability to scavenge hydrogen peroxide, which is attributed to the redox properties of Ce ions. The catalytic ability of Ce ions on hydrogen peroxide was verified by o-phenylenediamine experiments, which demonstrated that both cerium nitrate and CeZnHA can catalyze the decomposition of hydrogen peroxide and oxidize o-phenylenediamine, characterized by the gradual transformation of a colorless solution to a yellow solution (Fig. 1g). UV spectrophotometric experiments further demonstrated that CeZnHA catalyzed hydrogen peroxide exhibits corresponding characteristic peaks (Fig. 1h and i).

Next, we successfully prepared a PLA/GelMA electrospun film, which was then processed into a uniform short fiber solution using a high-speed homogenizer and subsequently freeze-dried to form a short fiber scaffold by UV cross-linking. From the appearance, the crosslinked short fiber scaffolds showed overall smaller shrinkage, and their color changed from colorless to light yellow (Fig. 2a). In addition, the cross-linked short fiber scaffolds demonstrated greater structural stability, maintaining their shape under magnetic stirring without collapsing (Fig. 2b). Furthermore, we successfully prepared homogeneous gelatin microspheres with controlled cross-linking strength, which depend on the EDC concentration, with a particle size of approximately 100 μm (Fig. 2c and d). SEM images recorded the morphology of CeZnHA-loaded gelatin microspheres, PLA/GelMA short fiber scaffolds, and composite scaffolds (Fig. 2e). The surface of CeZnHA nanoparticles-loaded gelatin microspheres exhibited a porous structure, facilitating both cell infiltration and the release of CeZnHA nanoparticles. The PLA/GelMA short fiber scaffolds showed a loose and porous structure with fiber diameters ranging from 500 to 1000 nm. After combining the two, the CeZnHA nanoparticles-loaded gelatin microspheres were uniformly distributed within the PLA/GelMA short fiber scaffolds, preserving the intrinsic structural features of the scaffolds. The cross-linked short fibers showed a slight decrease in diameter but a 20.4 % reduction in porosity compared to the uncross-linked fibers (Fig. 2f). The porosity of the hydrogel was lower than that of the short fiber group, measuring 35.53 % (Fig. 2g). Fourier transform infrared spectroscopy (FTIR) results confirmed that CeZnHA was successfully introduced into gelatin microspheres, as indicated by the presence of the characteristic PO_4^{3-} peak (Fig. 2h). The hydrophilicity of the scaffold is crucial for cell survival. The loose and porous short fiber scaffold exhibits excellent water absorption, enabling it to rapidly absorb biofluids in injured tissues, thus accelerating hemostasis and cellular infiltration of the wound. The maximum water absorption rate of the scaffold exceeded 960 % within 5 min and remained stable under mechanical force (Fig. 2i). An appropriate degradation rate is essential for orderly tissue healing. The PLA/GelMA short fiber scaffolds possessed a relatively slow degradation rate, with only 58 % degraded after 28 days (Fig. 2j). However, the CeZnHA-loaded gelatin microspheres were nearly completely degraded by 28 days, which was attributed to the weaker cross-linking of the EDC-crosslinked gelatin microspheres (Fig. 2k). This trend was confirmed by optical images of the degradation experiments, which showed that the CeZnHA-loaded gelatin microspheres maintained a stable morphology for the first three days. Extensive degradation began on the seventh day, with over 80 % of the microspheres degraded by the 21st day (Fig. 2l). This ensures that the system favors the maintenance of the body's intrinsic inflammatory response during the first 3 days, after which it begins to play an immunomodulatory role in suppressing the body's inflammation [20]. However, the inclusion of microspheres led to a decrease in the compressive strength and Young's modulus of the scaffold, likely due to the weak interaction between the microspheres and the fiber scaffold (Fig. S2).

In fact, the physicochemical properties of materials are highly correlated with immune cell activity, and considering the degradation rate of the material is crucial for directing immunomodulatory behavior. Polymers with a slow degradation rate effectively reduce the infiltration of inflammatory macrophages and promote the secretion of anti-inflammatory factors by immune cells, leading to wound healing, inhibition of scarring, and vascular maturation [35–37]. Therefore, designing polymer scaffolds with appropriate and adjustable degradation rates is ideal for balancing immune homeostasis and accelerating tissue regeneration. Considering the optimal osteogenic window of 4–8 weeks, we selected a stable C=C double bond of modified gelatin and PLA to form a short fiber scaffold. The resulting 58 % degradation rate at 4 weeks ensured the release of active substances and facilitated bone tissue growth. Gelatin, known for its excellent biocompatibility, has been widely used to deliver various bioactives. Glutaraldehyde is a classical chemical cross-linking agent that facilitates the formation of a stable three-dimensional network in gelatin through the Schiff base bond formed between the aldehyde group and hydroxylysine in gelatin [38]. However, its biotoxicity, leading to thrombosis, calcification, and poor endothelialization, is detrimental to immune modulation [39]. Therefore, we selected EDC, a biocompatible cross-linking agent with adjustable cross-linking strength, and finalized a concentration of 0.5 M. EDC cross-links the gelatin molecular chains to form amide bonds [40], with stable release of encapsulated nanoparticles beginning after 3 days. This delayed release ensures that high doses of nanoparticles are not prematurely exposed within the tissue, thereby maintaining *in vivo* biocompatibility.

2.3. Cell viability of mitochondrial rheostats

Mitochondrial rheostats scaffolds are used as bone implant materials and ensuring their cell viability is a prerequisite for successful treatment. Bone marrow mesenchymal stem cells (BMSCs) and macrophages are important cells that exert osteogenic and immunomodulatory functions, and their quantity and functional transformation determine bone healing. Therefore, we evaluated the cell viability of the scaffolds using live-dead staining, cytoskeletal staining, and cell proliferation assays (Fig. S3). The experiment groups included Control, FM, FM@HA, FM@ZnHA and FM@CeZnHA. First, calcein AM/PI staining was performed on co-cultured macrophages and BMSCs on days 1 and 3, respectively. The results indicated that macrophages and BMSCs maintained high cell viability with almost no dead cells. Notably, the FM@ZnHA and FM@CeZnHA groups demonstrated a significant proliferation-promoting effect on macrophages after 3 days of co-culture, with cell viability considerably higher than the other groups. However, no statistical difference was observed between the groups after co-culture with BMSCs. Then on day 3, the cytoskeleton of the co-cultured macrophages and BMSCs were stained separately, and the morphology of the scaffolds and cells was detected using phalloidin. Macrophages in the Control and FM groups became morphologically larger and extended irregular tentacles, characteristics consistent with the inflammatory macrophage phenotype. In contrast, macrophages in the FM@HA, FM@ZnHA, and FM@CeZnHA groups began to develop elongated pseudopods and exhibited a spindle-shaped morphology, consistent with anti-inflammatory macrophages (Figs. S3 and S4). Besides, there was no statistical difference in the morphology of BMSCs among the Control, FM, FM@HA, FM@ZnHA, and FM@CeZnHA groups,

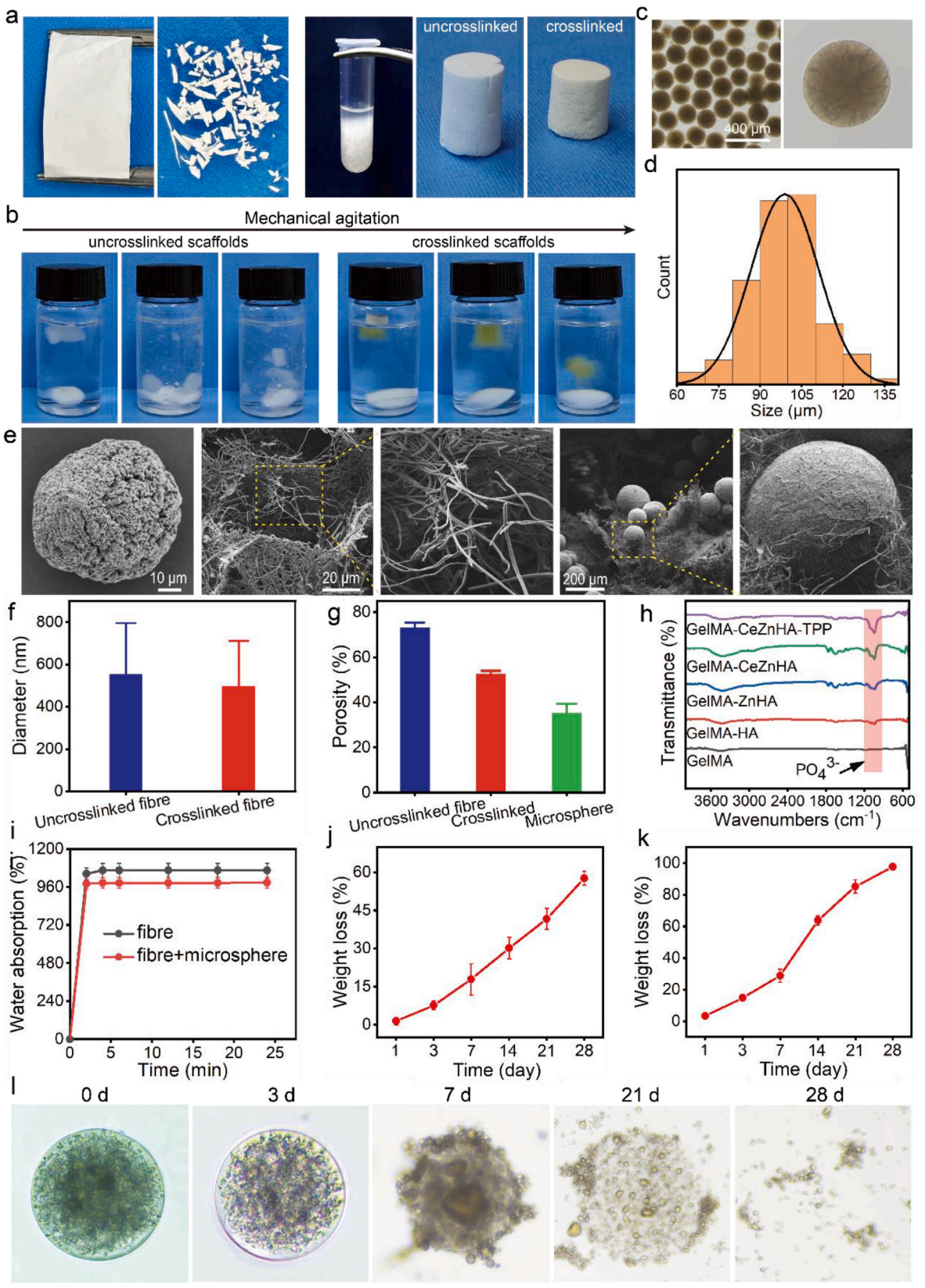

Fig. 2. a) Optical photographs of PLA/GelMA membranes and their crosslinked scaffolds. b) Mechanical stability of crosslinked and uncrosslinked PLA/GelMA scaffolds. c) Optical photographs of gelatin microspheres and their d) particle size distribution. e) SEM images of microspheres, PLA/GelMA, and PLA/GelMA/microspheres. f) Diameters of crosslinked and uncrosslinked fibers. g) The porosity of crosslinked fibers, uncrosslinked fibers, and microspheres. h) FTIR spectroscopy of PLA/GelMA, PLA/GelMA/HA, PLA/GelMA/ZnHA, PLA/GelMA/CeZnHAP, and PLA/GelMA/CeZnHAP-TPP. i) Water absorption of PLA/GelMA and PLA/GelMA/CeZnHAP. The 4-week degradation rate of j) PLA/GelMA and k) CeZnHAP. l) Optical photographs of degradation process of CeZnHAP. The abbreviations for PLA/GelMA, PLA/GelMA/HA, PLA/GelMA/ZnHA, and PLA/GelMA/CeZnHAP-TPP in subsequent experiments were FM, FM/HA, FM/ZnHA and FM/CeZnHAP, respectively.

all of which displayed a spindle-shaped morphology. In summary, the cell viability of our designed scaffolds remained high after co-culture with macrophages and BMSCs, meeting the requirements for subsequent experiments and normal bone implantation.

2.4. Mitochondrial rheostats target macrophage mitochondria and modulate their metabolites

To verify the mitochondrial targeting of CeZnHA nanoparticles, we conjugated FITC on the surface of CeZnHA nanoparticles and co-cultured them with macrophages for 12 h. As shown in Fig. 3a and b, the co-localization results indicated that CeZnHA nanoparticles with the green-fluorescent overlapped with mitochondria with the red-fluorescent as yellow signals and were widely distributed within the intracellular space, which proved that CeZnHA nanoparticles could be effectively internalized by macrophages and accumulated around mitochondria (mitochondrial stained with Mito-Tracker Red and CeZnHA labeled with fluorescein isothiocyanate (FITC)). The mitochondrial targeting function of CeZnHA nanoparticles was further confirmed by stereoscopic scanning of macrophages and 3D image reconstruction using laser confocal microscopy. Subject to size limitation, TPP-modified nanoparticles targeted and aggregated around the outer

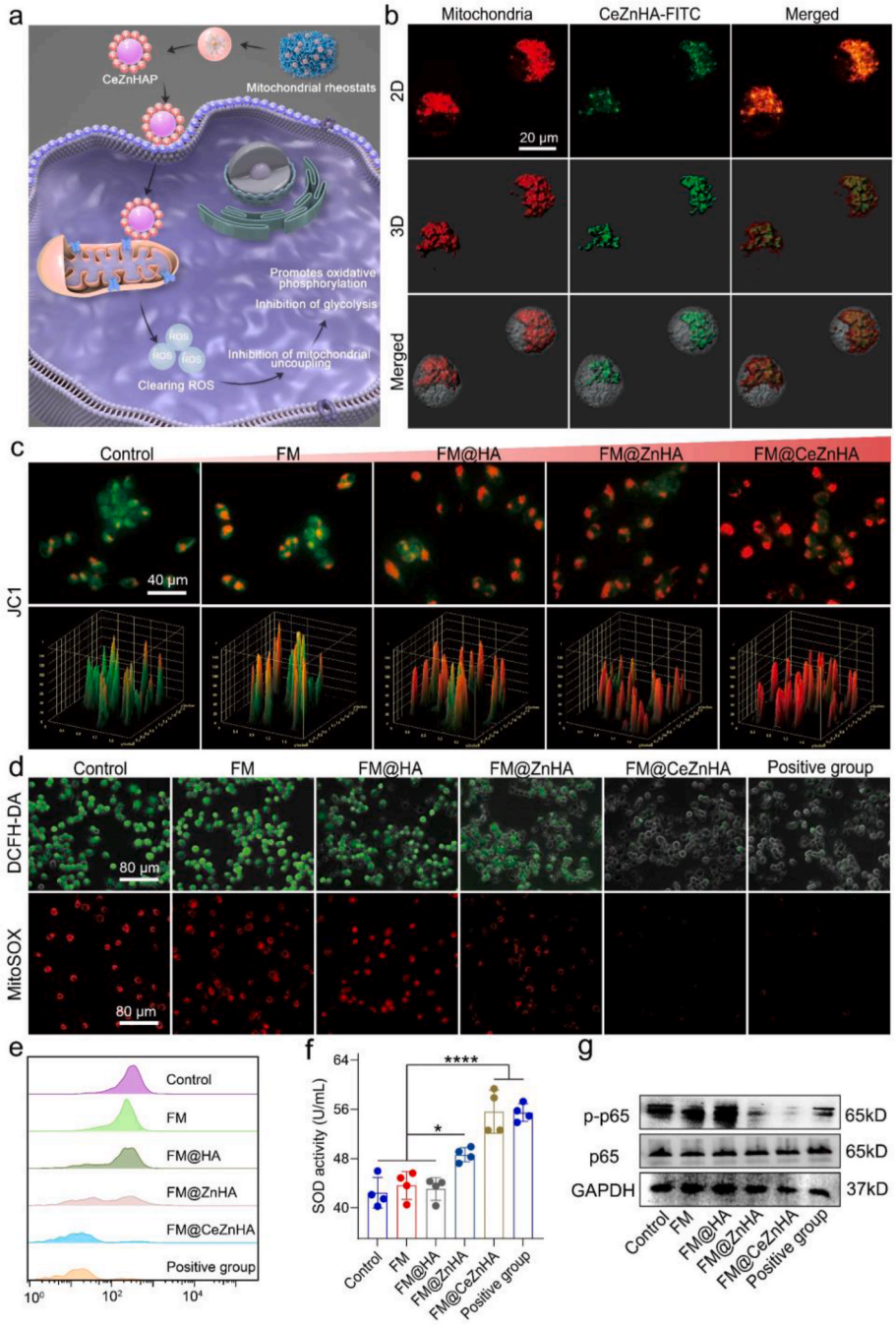

Fig. 3. a) Schematic diagram of CeZnHA targeting mitochondria. b) Laser confocal images of CeZnHA targeting macrophage mitochondria. Changes of c) mitochondrial membrane potential, d) DCFH-DA and MitoSOX fluorescence, e) ROS flow cytometry and f) SOD activity of macrophages in the different groups stimulated by LPS conditions (500 ng/mL). g) Validation of NF-κB p65 pathway activation using western blots. ns means no significant difference, * means $p < 0.05$, *** means $p < 0.001$, **** means $p < 0.0001$.

mitochondrial membrane to scavenge ROS from the inner mitochondrial membrane and cytoplasm by releasing metal ions. 5,5′,6,6′-Tetrachloro-1,1′,3,3′-tetraethyl-imidacarbocyanine iodide (JC-1) was conducted as a visual fluorescent molecule to evaluate mitochondrial membrane potential. When the mitochondrial membrane potential is elevated, JC-1 monomers form red fluorescent polymers in the mitochondrial matrix; otherwise, they exhibit green fluorescence. The relative ratio of red to green fluorescence is an important indicator of mitochondrial depolarization. JC-1 staining of macrophages after co-culture with the scaffolds revealed that, in the presence of lipopolysaccharide (LPS), macrophage mitochondria in the Control and FM groups showed many green fluorescent JC-1 monomers, whereas macrophage mitochondria in the FM@HA, FM@ZnHA and FM@CeZnHA groups were detected with a higher number of red fluorescent JC-1 aggregates, indicating an upward trend (Fig. 3c). It was shown that LPS-stimulated macrophage metabolism shifted from adenosine triphosphate (ATP) production via oxidative phosphorylation to glycolysis, with a concomitant increase in succinate levels. Enhanced mitochondrial oxidation of succinate and the rise in mitochondrial membrane potential collectively drove the production of mitochondrial ROS [26]. ROS can reprogram macrophages from an anti-inflammatory phenotype (M2) to a pro-inflammatory phenotype (M1) [25]. Elevated intracellular ROS, mainly of mitochondrial origin, translocate NF-κB into the nucleus and induce its phosphorylation, activating inflammatory macrophages [41]. This process also activates the p38 mitogen-activated protein kinases (p38 MAPK) signaling pathway, leading to lipid droplet accumulation, which further exacerbates intracellular lipid peroxidation and suppresses the anti-inflammatory macrophage phenotype [42]. Therefore, scavenging mitochondrial ROS is an effective strategy for reprogramming the metabolic mode of macrophages. To assess the ability of the scaffolds to scavenge LPS-induced macrophage ROS, we used DCFH-DA and MitoSOX fluorescent probes to detect ROS expression levels in macrophages. A large amount of ROS with high fluorescence intensity was present in the macrophage intracellular and mitochondria under LPS stimulation in the control and FM groups. The macrophage intracellular and mitochondrial ROS levels were significantly reduced in the FM@ZnHA group, and the overall ROS expression in the FM@CeZnHA group was the lowest, which was comparable to that of the positive control group, suggesting that the FM@CeZnHA group could reduce the oxidative stress of the cells induced by LPS to return to the normal level (Fig. 3d). Flow cytometry results also confirmed that the FM@CeZnHA group significantly reduced ROS levels in macrophages (Fig. 3e). In addition, the SOD activities of the FM@ZnHA group, the FM@CeZnHA group and the positive group were significantly higher, which also implies that they have a strong ability to scavenge ROS (Fig. 3f). The Western blot results showed that p-p65 protein expression was reduced in the FM@ZnHA group, FM@CeZnHA group and the positive group compared to the other groups, implying that the NF-κB p65 pathway is ROS-dependent (Fig. 3g). It has been shown that Zn is a key metal cogroup of various enzymes that can polarize macrophages into an anti-inflammatory phenotype and induce the secretion of anti-inflammatory factors [43]. Additionally, elemental Zn has been shown to favor the restoration of damaged mitochondrial networks and morphology, helping to counteract the abnormal mitochondrial morphology caused by elevated ROS [44,45]. Elemental Ce is highly efficient in scavenging intracellular ROS, attributed to its rapid Ce^{3+} and Ce^{4+} transitions. Ce^{3+} scavenges O^{2-} and ·OH, which are associated with inflammatory responses and cell death by mimicking superoxide dismutase, while Ce^{4+} scavenges H_2O_2 by mimicking catalase [46,47].

Inorganic nanoparticles can be internalized and reprocessed by immune cells, thereby regulating the fate and function of these cells. On the one hand, the metabolic activity of immune cells is affected by the dose of nanoparticles. An excess of nanoparticles induces immune cells to secrete inflammatory factors, leading to an irreversible inflammatory response and exacerbating tissue damage. On the other hand, the inherent physicochemical properties of nanoparticles can regulate the metabolic processes of immune cells. During internalization, nanoparticles can mimic apoptosis processes, activating immune cells to perform scavenging functions. For example, Yan et al. targeted adipocytes and disguised them as apoptotic cells using gold nanobipods (PAAu BPs), which activated macrophages to clear the adipocytes while reprogramming inflammatory macrophages toward an anti-inflammatory phenotype, thereby enabling the treatment of obesity through an immunotherapeutic strategy [48]. The copper-based nanoplatform (BCMD) constructed by Huang et al. released Cu^{2+} in the acidic tumor environment, where it was metabolically reduced to Cu^{+}, increasing the tumor's oxygen content. This contributed to the copper-induced apoptosis process and exacerbated T-lymphocytes infiltration in glioblastomas, reversing the immune-suppressive microenvironment, enhancing tumor-killing immunity, and enabling immunotherapy [49]. Additionally, nanoparticles can act as antioxidants to reduce oxidative stress in immune cells, thereby guiding cellular functional shifts. Yang et al. constructed an in situ-synthesized manganese porphyrin with an active manganese site similar to the metal sites of natural superoxide dismutase (SOD) and catalase. This compound exhibited high antioxidant effects, promoting the polarization shift of M1 macrophages to an anti-inflammatory M2 phenotype [50].

Given that macrophage phenotypes are mainly regulated by mitochondrial function and related metabolism, we investigated the changes in mitochondrial morphology and metabolites induced by CeZnHA after its entry into macrophages. As shown in Fig. 4a–c, macrophage mitochondria exhibited increased electron density, crumpling, and volume reduction upon LPS stimulation. Under the protection of CeZnHA, macrophage mitochondria resisted LPS stimulation, and the electron density and volume were close to those of untreated macrophages, which may be related to the elimination of oxidative stress. Cellular metabolites are important indicators of phenotype and function. Therefore, to further investigate the effects of scaffolds on mitochondrial metabolites in macrophages, we used liquid chromatography-tandem mass spectrometry (LC-MS/MS) to analyze the metabolites of macrophages after co-incubation with DMEM medium, DMEM medium containing LPS, and scaffolds-impregnated DMEM medium. Enhanced glycolysis and unbalanced tricarboxylic acid (TCA) circulation are associated with the polarization of pro-inflammatory M1-like macrophages, whereas anti-inflammatory M2-like macrophages are characterized by glutamine- and fatty acid-fueled mitochondrial respiration [3]. The results showed 20 differentially expressed metabolites between the LPS and the Control groups, with 14 related to the TCA cycle and 6 related to glycolysis. Thermograms and quantitative analyses revealed that after co-incubation with FM@CeZnHA scaffolds, several key glycolysis metabolites, such as D-Fructose 1,6-bisphosphate, B-D-Fructose 6-phosphate, D-Glucose 6-phosphate, lactic acid, 3-Phospho-D-glycerate, and phosphoenolpyruvic acid, were significantly lower than in the LPS group and not significantly different from the Control group. Regarding the TCA cycle, thermogram and quantitative analysis showed that after co-incubation with FM@CeZnHA scaffolds, acetyl coenzyme A, adenosine 5′-diphosphate, adenosine 5′-triphosphate and citric acid were immensely higher than in the LPS group and not statistically different from the Control group. These data suggest that FM@CeZnHA scaffolds may reduce cellular glycolysis and increase mitochondrial TCA cycle metabolites associated with M2 polarization after co-incubation with macrophages (Fig. 4d and e, S8 and S9). Extracellular flux analysis further validated the effect of FM@CeZnHA scaffolds on the metabolic status of macrophages. The Control group consisted of normal macrophages without any treatment. The basal respiration, maximal respiration, and OCR/ECAR ratio of cells in the FM@CeZnHA scaffold group were notably higher than in the LPS group and not remarkably different from the Control group (Fig. 4f and S7), indicating that FM@CeZnHA had a better oxidative phosphorylation efficiency. Of these, FCCP is a decoupling agent that disrupts the proton gradient and mitochondrial membrane potential, and oxygen consumption by mitochondrial complex IV is maximized, so that FCCP excites a curve of

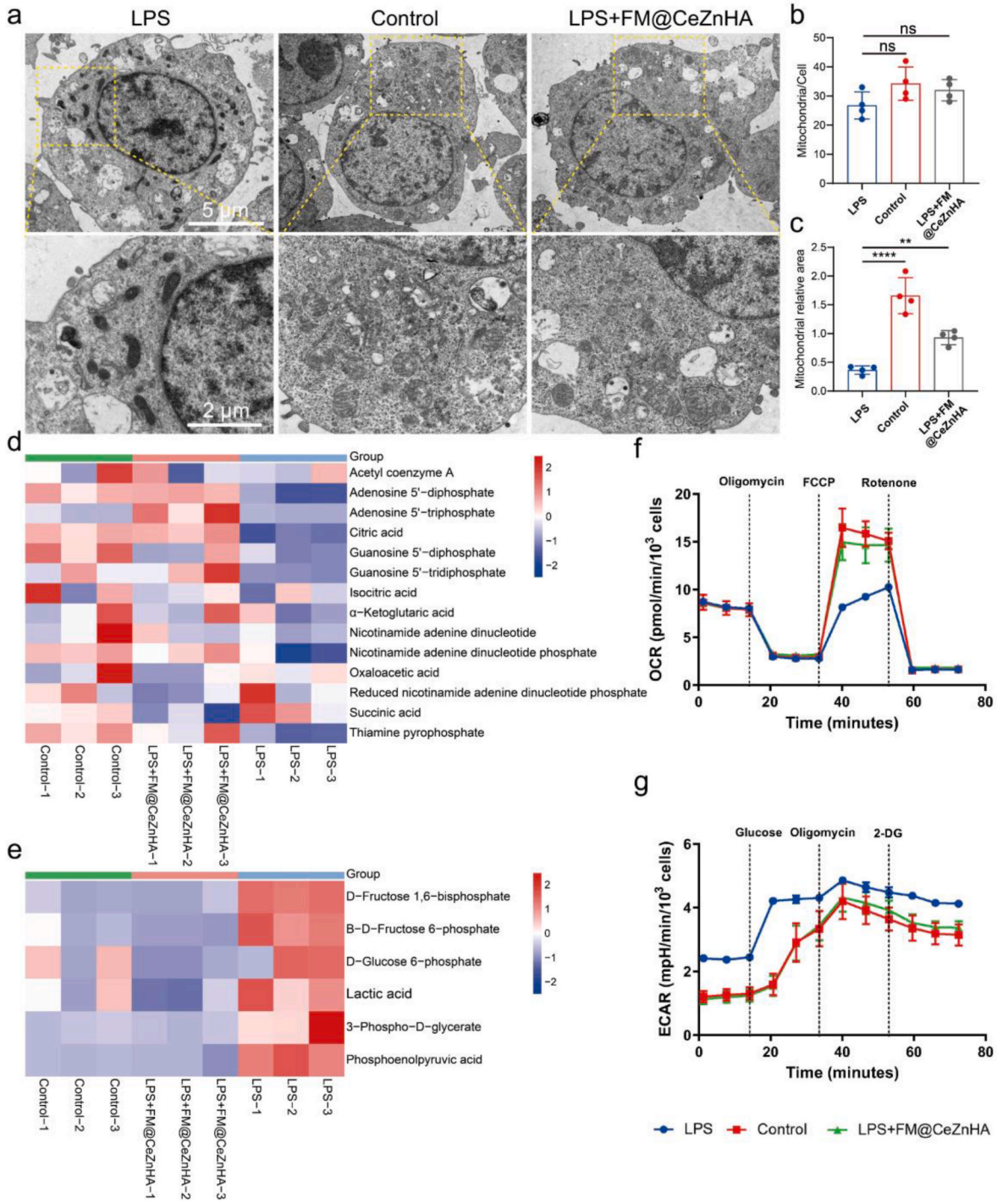

Fig. 4. Mitochondrial metabolic status after co-culture of scaffolds and macrophages. a) SEM images of mitochondrial morphological changes of macrophages in different groups (LPS, Control, and LPS + FM@CeZnHAP). Control group represents macrophages without LPS stimulation. b) Statistical plots of mitochondrial number and c) relative area in macrophages. Thermograms of cellular d) oxidative phosphorylation metabolites and e) glycolytic metabolites were detected by LC-MS/MS after different groups of treated macrophages. f) Real-time OCRs of macrophages in response to sequential treatment with Oligo, FCCP, and rotenone (f, cell mitochondrial stress test). g) Real-time ECARs of macrophages in response to sequential injection of glucose, Oligo, and 2-DG (g, glycolysis stress test). ns means no significant difference, * means $p < 0.05$, *** means $p < 0.001$, **** means $p < 0.0001$.

maximal cellular respiratory capacity [24]. Meanwhile, real-time extracellular acidification rates (ECARs) of macrophages proved that FM@CeZnHA scaffold-treated macrophages notably reduced the rate of ECARS, suggesting that it inhibited the process of cellular glycolysis, and the massive secretion of lactic acid in LPS group increased the rate of ECARS (Fig. 4g). Among them, the significant increase of OCE/ECAR indicated that macrophages were more dependent on mitochondrial metabolism after FM@CeZnHA treatment.

2.5. *In vitro immunomodulatory effects of mitochondrial rheostat scaffolds*

To further validate the immunomodulatory function of the scaffold on macrophages, the phenotypic shift, expression of inflammatory and

anti-inflammatory factors, and metabolic status of macrophages were assessed using immunofluorescence staining, flow cytometry, enzyme immunoassay, and real-time fluorescence quantitative PCR. Immunofluorescence analysis was performed to assess the expression of pro-inflammatory phenotype (Cluster of Differentiation 86, CD86) and anti-inflammatory phenotype (Cluster of Differentiation 206, CD206) markers in macrophages. Macrophages co-cultured with FM@HA, FM@ZnHA, and FM@CeZnHA scaffolds expressed less CD86 and more CD206 compared to the Control and FM groups (Fig. 5a and S5). Flow cytometry data confirmed that the proportion of anti-inflammatory macrophage was notably higher in the FM@HA, FM@ZnHA and FM@CeZnHA groups (Fig. 5c). Further, mRNA expression of genes related to anti-inflammatory macrophages and pro-inflammatory macrophages was detected using qPCR. The results showed that macrophages in the FM@HA, FM@ZnHA and FM@CeZnHA groups significantly upregulated genes related to the anti-inflammatory phenotype (arginase 1 (Arg-1) and IL-10) and downregulated genes associated with the pro-inflammatory phenotype (interleukin-1 beta (IL-1β) and inducible nitric oxide synthase (INOS)). These effects were notably stronger in the FM@CeZnHA group, which had the most pronounced impact on promoting macrophage polarization to an anti-inflammatory phenotype (Fig. 5d). Analysis of inflammatory and anti-inflammatory factors secreted by macrophages is an effective way to assess their metabolic status. After 24 h of co-culture with the scaffolds macrophages supernatants were collected and analyzed for TNF-α and IL-10 concentrations using enzyme immunoassay. The results showed that the FM@HA, FM@ZnHA and FM@CeZnHA groups significantly promoted the secretion of anti-inflammatory factors by macrophages while decreasing pro-inflammatory factors, contributing to the polarization of macrophages toward an anti-inflammatory phenotype instead of a pro-inflammatory phenotype (Fig. 5b). The metabolic status of macrophages after scaffold culture was further analyzed using quantitative polymerase chain reaction (qPCR), examining the expression of genes related to macrophage glycolysis and oxidative phosphorylation (Fig. 5d). These data indicated that the FM@HA, FM@ZnHA and FM@CeZnHA groups inhibited glycolytic in macrophages while promoting oxidative phosphorylation in mitochondria.

2.6. Immuno-osteogenic differentiation modulation properties of mitochondrial rheostats

To assess macrophage immunomodulation-mediated osteogenic differentiation, we stimulated BMSCs by placing the scaffolds co-cultured with macrophages in conditioned medium and subjected them to alkaline phosphatase (ALP) staining and alizarin red staining at 7 and 14 days, respectively (Fig. 6a). The results of ALP staining described that, compared with the Control and FM groups, the staining depth of the FM@HA, FM@ZnHA and FM@CeZnHA groups was deeper (Fig. 6b). The expression level of alkaline phosphatase in the FM@CeZnHA group was 5.33, 6.66, 1.80 and 1.36 times that of the Control, FM, FM@HA and FM@ZnHA (Fig. S6a). Alizarin red staining proved that more calcium nodules appeared in the FM@CeZnHA group, and their colors were darker (Fig. 6c). Quantitative data showed that the mineralization degree of the FM@CeZnHA group was 2.3, 2.03, 1.47 and 1.18 times that of the Control, FM, FM@HA and FM@ZnHA, respectively (Fig. S6b). Furthermore, we used immunofluorescence staining and quantitative real-time fluorescence PCR to evaluate the relative expression levels of osteogenesis-related proteins and genes in BMSCs co-cultured with the scaffold on day 7. Immunofluorescence pictures of osteocalcin (OCN) and collagen type I (COL-I) on day 7 showed that the FM@CeZnHA group exhibited stronger osteogenic differentiation compared to the other groups, and the quantitative data also supported these findings (Fig. 6d and e and S6c). In addition, we detected the relative expression of osteogenesis-related genes at the molecular level, and the qPCR results confirmed that BMSCs in the FM@CeZnHA group significantly up-regulated the expression levels of the osteogenesis-related genes (ALP, runt-related transcription factor 2 (RUNX2), COL-I, OCN, and osteopontin (OPN)) and the trend was consistent with the immunofluorescence intensity of OCN and COL-I (Fig. 6d). In summary, the osteogenic differentiation experiments demonstrated that the FM@CeZnHA scaffolds regulated macrophage polarization and its metabolites, thereby contributing to osteogenic differentiation through an immune microenvironment-mediated process.

2.7. Immuno-osteogenic properties of mitochondrial rheostats in vivo

Based on the above results, the mitochondrial rheostats targeted mitochondria, modulated macrophage glucose metabolism, induced a shift to an anti-inflammatory phenotype, and promoted the osteogenic differentiation of BMSCs *in vitro*. To evaluate bone ingrowth more intuitively, micro-CT scans and three-dimensional reconstructions of the femoral condylar defect site were performed in rats at 2 and 4 weeks postoperatively (Fig. 7a and b). At 2 weeks, there was less neoplastic bone tissue in the Control and FM groups, while neoplastic bone tissue in the FM@HA, FM@ZnHA, and FM@CeZnHA groups gradually ingrew, attributed to the excellent osteoconductivity of HA. However, the overall bone density at the defect site was lower. At 4 weeks, the Control and FM groups still maintained less new bone at the defect, while the FM@HA, FM@ZnHA, and FM@CeZnHA groups achieved complete defect closure and significant new bone tissue growth, with an increase in overall bone density compared to 2 weeks. Quantitative data on bone density, trabecular thickness, trabecular separation, and new bone volume showed that the FM@CeZnHA group had a faster rate of osteogenesis and superior bone quality (Fig. 7c). Based on the imaging data, we hypothesized that the scaffold, in addition to filling the defect in the early stage of injury, could also promote cell migration and osteogenic differentiation toward the scaffold due to the osteoconductive and osteoinductive effects of HA. Notably, the immunomodulatory effects of Zn and Ce ions on macrophages played a crucial role in maintaining the early immune microenvironment, thereby facilitating the late bone regeneration process [51,52].

The early and late osteogenic capacity of the scaffold was further assessed using histologic evaluation of the defect site with masson trichrome and hematoxylin-eosin staining (Fig. 8a). At 2 weeks postoperatively, all groups showed varying degrees of unhealed defects, with the Control and FM groups showing less new bone growth due to the lack of osteoconductive and osteoinductive properties. The FM@HA, FM@ZnHA, and FM@CeZnHA groups promoted cell migration to the defect area and osteogenic differentiation, with the FM@ZnHA and FM@CeZnHA groups exhibiting well-arranged collagen fibers, higher bone maturation, and markedly higher osteogenic capacity than the remaining groups. At 4 weeks postoperatively, the defect areas in the Control and FM groups were still not completely healed, likely due to the poor early immune microenvironment and osteoconduction. The newly formed bone tissues in the FM@HA, FM@ZnHA, and FM@CeZnHA groups completely filled the defect areas, with the thickness of the trabeculae, the degree of bone separation, and the degree of bone maturation being significantly better than those in the other groups (Fig. 8b and c). Although the bone defect site was completely closed in the FM@HA group, the bone density was lower than that in the FM@ZnHA and FM@CeZnHA groups. In the early stages of macrophage infiltration, HA was unable to accurately target macrophage mitochondria to modulate macrophage metabolic processes, resulting in inadequate early immune microenvironment regulation at the defect site. The weaker immune regulatory capacity failed to promote the timely transformation of macrophages into an anti-inflammatory phenotype, leading to the reduced osteogenic capacity observed in the FM@HA group.

Temporal shifts between inflammatory and anti-inflammatory macrophage phenotypes in the early injury microenvironment are critical for efficient bone healing and bone quality. We modulated the

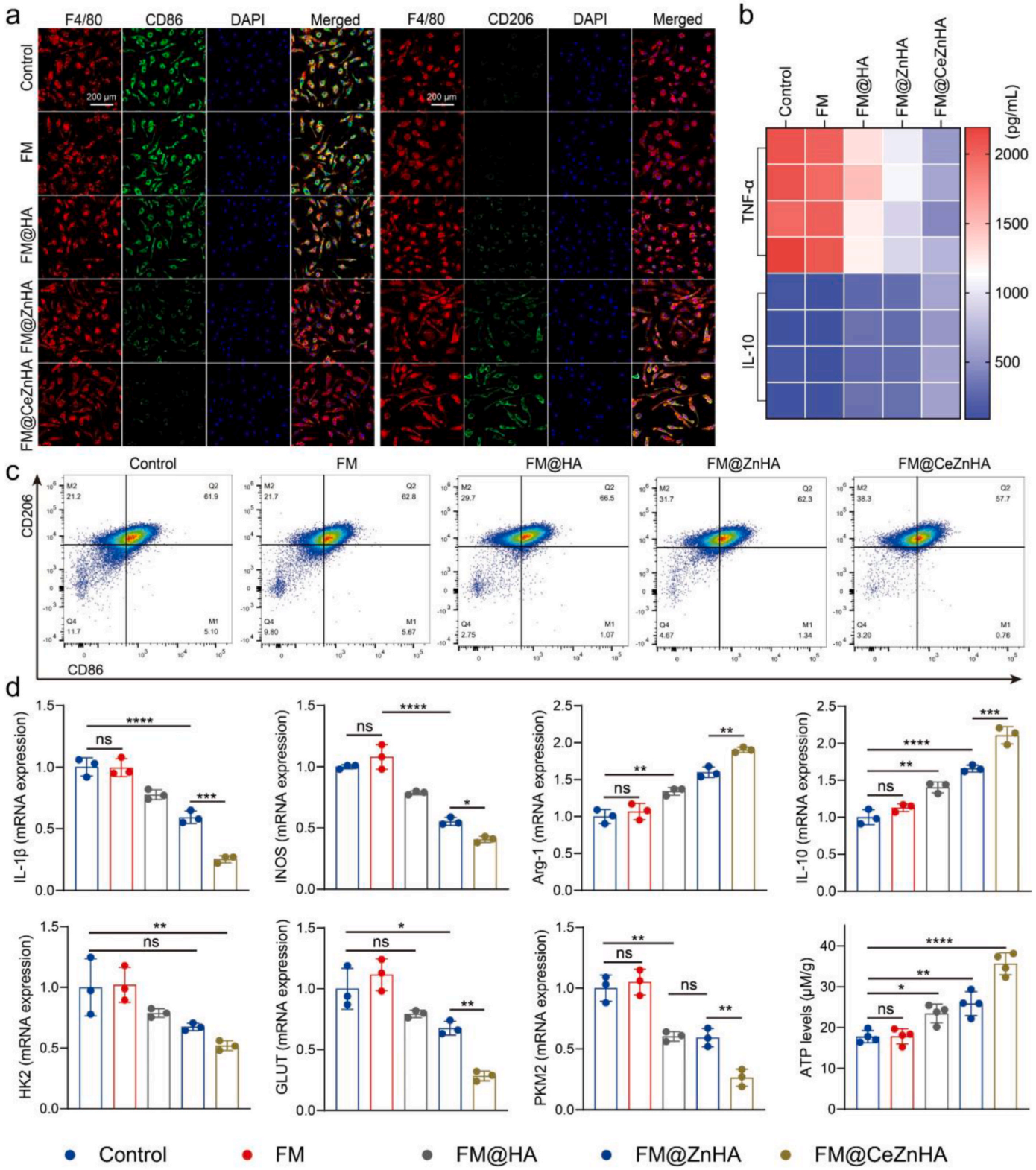

Fig. 5. a) Immunofluorescence expression levels of CD86 and CD206 in macrophages co-cultured with scaffolds (500 ng/mL LPS). b) Heat map of cytokine secretion levels (TNF-α and IL-10) after co-culture of scaffolds with macrophages. c) The amount of M1 and M2 was detected by flow cytometry after macrophages were co-cultured with scaffolds. d) The expression levels of macrophage related genes (IL-1β, INOS, Arg-1 and IL-10) and glycolysis-related genes (HK2, GLUT and PKM2) were detected by qPCR after scaffold-macrophage co-culture and expression levels of ATP after scaffold-macrophage co-culture. ns means no significant difference, * means $p < 0.05$, *** means $p < 0.001$, **** means $p < 0.0001$.

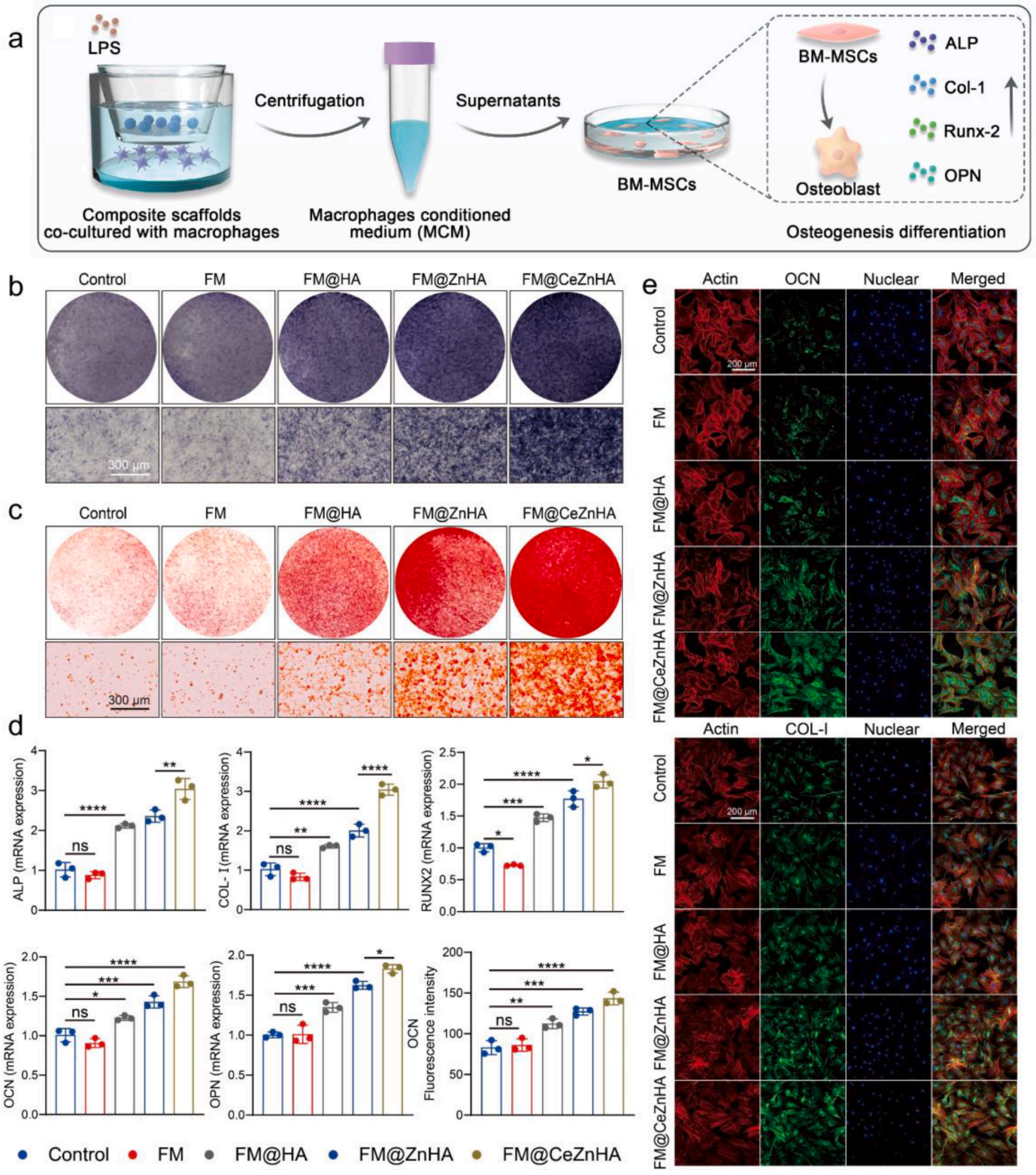

Fig. 6. a) Schematic diagram of macrophage conditioned medium regulating osteogenic differentiation of BMSCs. b) Alkaline phosphatase and c) alizarin red staining after scaffold-macrophage co-culture. d) The expression levels of osteogenesis-related genes (ALP, COL-I, RUNX2, OCN, and OPN) were detected by qPCR after scaffold-macrophage co-culture and quantitative analysis of immunofluorescence staining of OCN were detected by image J. e) Immunofluorescence staining of OCN and COL-I after scaffold-macrophage co-culture. ns means no significant difference, * means $p < 0.05$, *** means $p < 0.001$, **** means $p < 0.0001$.

functional shift of macrophages in the early bone injury microenvironment by releasing CeZnHAP nanoparticles from the scaffold. Surface markers of macrophages around the scaffolds were detected by immunofluorescence staining at 1 week postoperatively. The results revealed an obvious growth in anti-inflammatory macrophages at bone defects in the FM@HA, FM@ZnHA, and FM@CeZnHA groups, with upregulation of the specific marker CD206 and downregulation of INOS expression (Fig. 9a). Quantitative data showed that the proportion of anti-

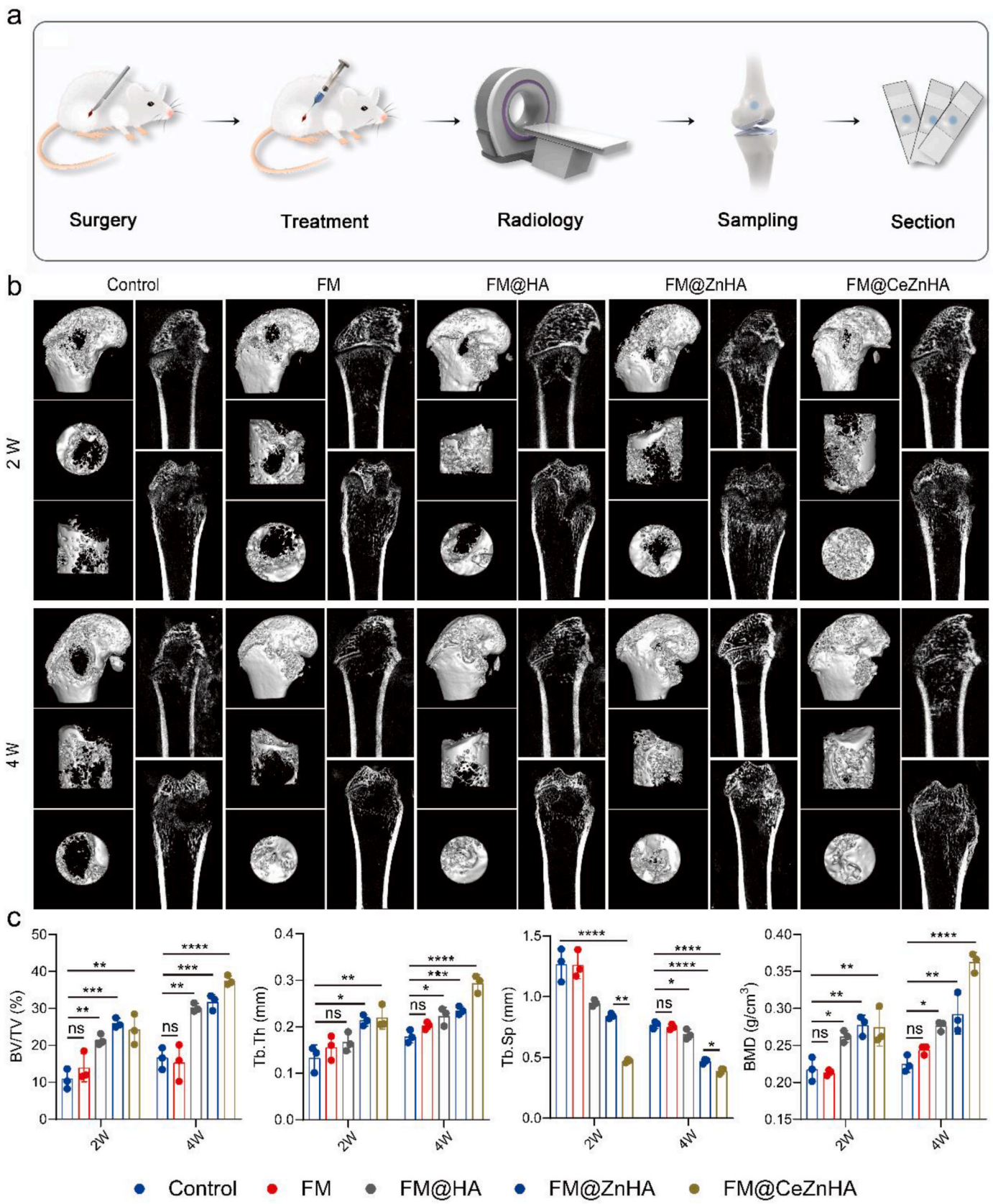

Fig. 7. a) Three-dimensional reconstruction of femoral condylar defects in rats 2 and 4 weeks after scaffold implantation. b) Micro-CT imaging and c) statistical analysis (BV/TV, Tb.Th, Tb.Sp and BMD) were performed to evaluate bone regeneration. ns means no significant difference, * means $p < 0.05$, *** means $p < 0.001$, **** means $p < 0.0001$.

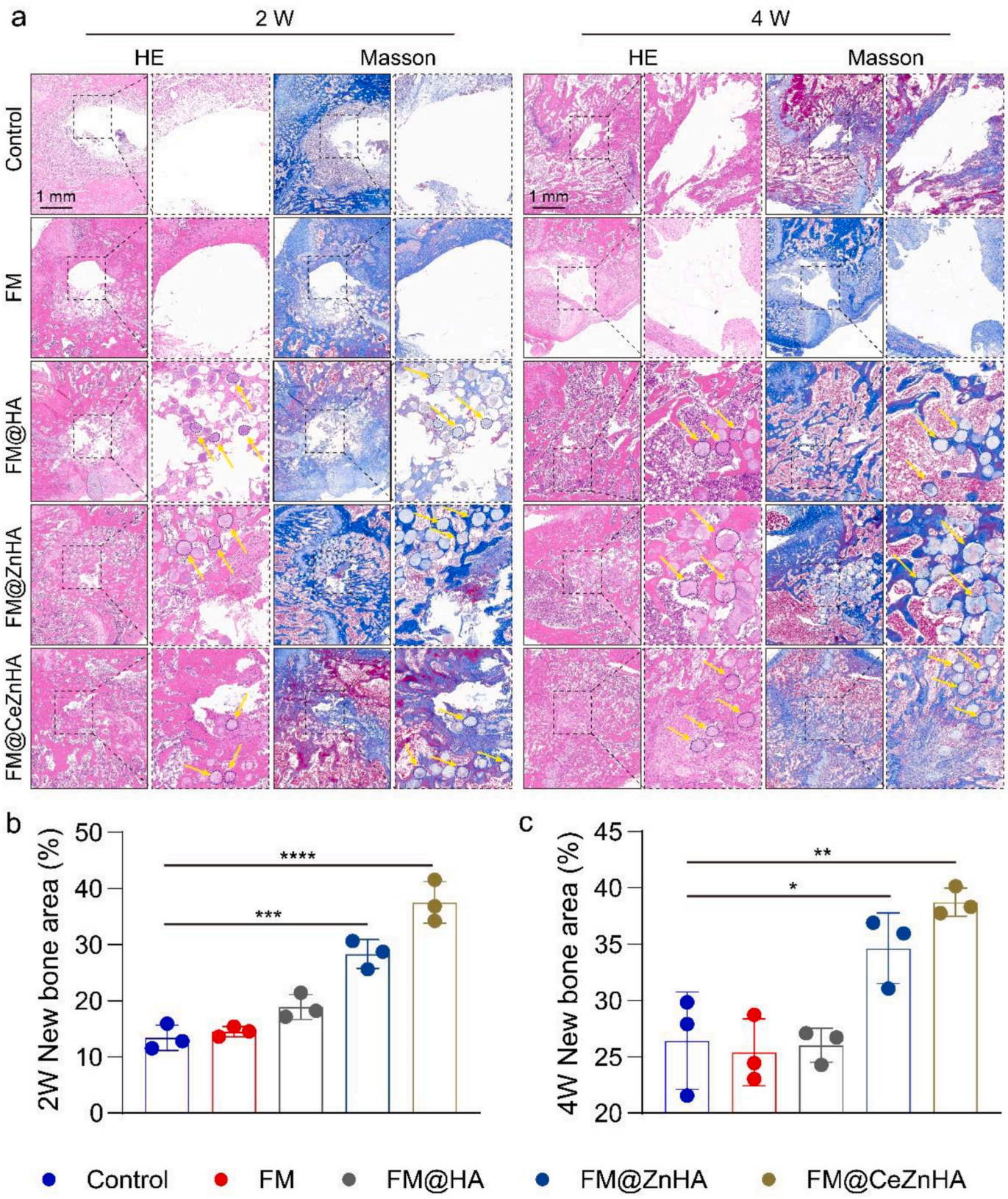

Fig. 8. a) HE and Masson staining of the scaffold-implanted femoral condylar defect at 2 and 4 weeks; the position of the yellow arrows in the figure shows the ossification centers formed by hydrogel microspheres. Quantitative analysis of the area of neoplastic bone at the scaffold-implanted femoral condylar defect site at b) 2 and c) 4 weeks. The above-mentioned statistical procedures were completed using image J. * means $p < 0.05$, *** means $p < 0.001$, **** means $p < 0.0001$.

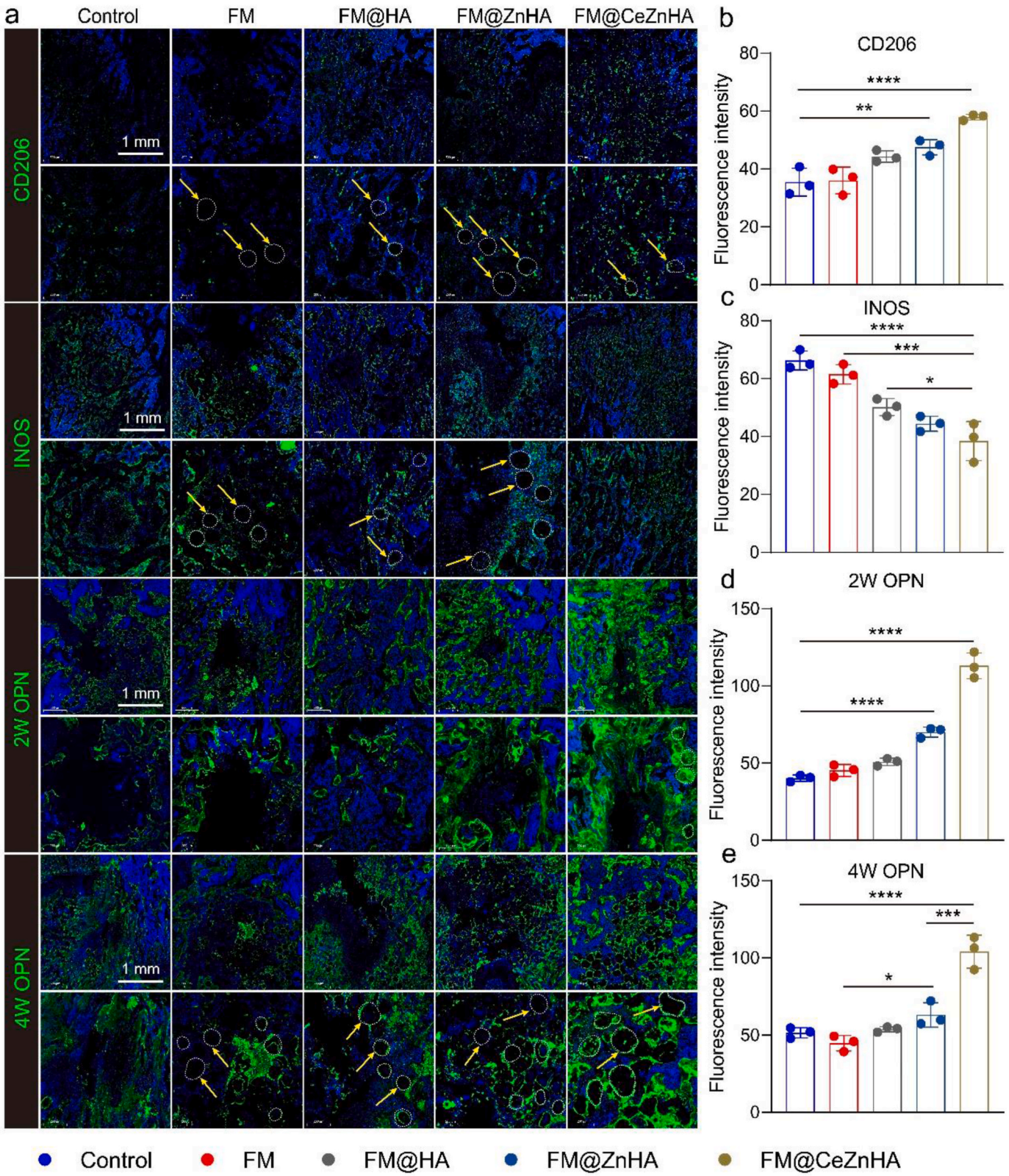

Fig. 9. a) The immunofluorescence expression levels of CD206 and INOS at 1 week and OPN at 2 and 4 weeks after scaffold implantation in femoral condylar defect. Quantitative analysis of b) CD206 and c) INOS expression levels at 1 week and OPN at d) 2 and e) 4 weeks after scaffold implantation in a femoral condylar defect. The above-mentioned statistical procedures were performed using image J. The white circles and yellow arrows in the figure represent the ossification centers formed by hydrogel microspheres. * means $p < 0.05$, *** means $p < 0.001$, **** means $p < 0.0001$.

inflammatory macrophages in the FM@HA, FM@ZnHA, and FM@CeZnHA groups was 1.31, 1.61, and 1.63 times higher than that in the Control, respectively (Fig. 9b). Additionally, the Control and FM groups exhibited higher levels of inflammatory macrophages compared to the other groups, with the FM@CeZnHA group showing the least infiltration of inflammatory macrophages. This may be attributed to CeZnHA's targeting of macrophage mitochondria for ROS scavenging, which promotes the transformation of macrophages into an anti-inflammatory rather than an inflammatory phenotype (Fig. 9c). To further determine the immunomodulatory role of macrophage functional shifts on bone regeneration, the expression of osteogenesis-related protein (OPN, an important bone matrix protein closely related to bone formation and development) was evaluated by immunofluorescence at 2 and 4 weeks after scaffold transplantation. The results indicated that OPN expression was vastly increased in the FM@HA, FM@ZnHA, and FM@CeZnHA groups compared to the Control and FM groups (Fig. 9a, d and 9e).

Based on the above experimental results, it can be seen that our material system resembles a "mitochondrial rheostat" at the site of bone defects, which regulates macrophage function and promotes tissue regeneration in a controlled and graded manner. On the one hand, the system acts as a "mitochondrial rheostat" by regulating macrophage mitochondrial metabolism and oxidative reduction, which targets the removal of ROS from macrophage mitochondria, balances their glycolysis and oxidative phosphorylation levels, and promotes their polarization to M2, shaping an anti-inflammatory microenvironment conducive to bone regeneration. On the other hand, the "mitochondrial rheostat" regulates the release of cytokines from macrophages through mitochondrial metabolic reprogramming, which activates the immune-regenerative cascade, accelerates the osteogenic differentiation of BMSC and promotes the repair of bone defects.

This study still faces many challenges: (1) The above animal experimental model is based on a non-critical defect model and is not fully applicable to other critical orthopaedic defects. (2) The longevity and integration of FM@CeZnHA *in vivo* should be explored over longer experimental periods (six months to two years) to assess chronic inflammatory responses, nanoparticle accumulation and metabolism. (3) The long-term biocompatibility and bioactivity of FM@CeZnHA should be evaluated in comparison to clinical-grade materials or approved scaffolds used for bone repair. (4) Consistency of biomaterial properties (e.g., composition, structure, mechanical properties), process standardisation and reproducibility are important issues to be addressed in scale-up production for clinical applications. (5) Explore how the immune response to scaffolds as foreign materials will affect their long-term success. In addition to immunometabolic abnormalities under pathological conditions, biomaterials themselves, as foreign substances, pose the same challenge to the natural immune system. Structural, compositional, and physicochemical signaling stimuli of biomaterials induce changes in the metabolic behavior of immune cells, and such metabolic shifts and metabolites may activate relevant signaling pathways and influence other cellular behaviors, which include modulation of cellular differentiation for regeneration, e.g., promotion of osteogenic differentiation of BMSCs and vascularization of endothelial cells. Conversely, altered immune cell behavior may also lead to excessive inflammatory responses, formation of fibrous encapsulation and scarring, and impeded tissue regeneration. Therefore, traditional orthopedic grafts based on biocompatibility as a criterion are insufficient. Understanding how biomaterials manage immune responses in unnatural states remains a focus of future research, which will guide the long-term success and clinical application of orthopedic biomaterials.

3. Conclusion

In summary, our study demonstrated that mitochondrial rheostats affect macrophage functional transitions by regulating glucose metabolism. The dual degradation rate mitochondrial rheostats rapidly released CeZnHA in the early stage, targeting macrophage mitochondria and scavenging ROS, which reduced macrophage glycolysis, enhanced oxidative phosphorylation, and prompted macrophage reprogramming to an anti-inflammatory phenotype. Additionally, the short-fiber scaffold provided a stable ossification platform in the later stages, accelerating the formation of ossification centers in hydrogel microspheres that responded to the immune response, ultimately achieving efficient bone regeneration. Therefore, the transformation of macrophage glucose metabolism guided by mitochondrial rheostats represents a highly effective immune response strategy, providing a new perspective for developing immune strategies for bone regeneration.

4. Experimental methods

Materials: PLA (Mw = 80,000–100,000), 1,1,1,3,3,3-hexafluoro-2-propanol (HFIP), EDC, N-Hydroxy succinimide (NHS), calcium nitrate, zinc nitrate, cerium nitrate, 3-carboxypropyl triphenylphosphonium bromide were purchased from Aladdin Biochemistry and Technology Company Limited, Shanghai. All other chemical reagents were obtained from Sigma-Aldrich.

Preparation and characterization of mitochondrial rheostats: In this study, Zn-doped HAP nanoparticles (Ca:Zn:P = 9:1:5.99) were prepared via the co-precipitation method, then 500 mg of PVA was used as a template agent, and 20 mL of hexamethylenetetramine (0.5 mM) was used as the alkaline solution to induce the deposition of 5 mL of cerium nitrate (0.5 mM) on 1 g of HAP, resulting in Ce/Zn-doped HAP. Ce/Zn-doped HAP was further amino functionalized by using 5 mL of 5 % APTES in hexane solution and then grafted 20 mg of 3-carboxypropyl triphenylphosphonium bromide in ethanol solution by an amide reaction to form CeZnHAP. The physical phase, morphology, elemental distribution, and elemental valence states of the nanoparticles were characterized using an X-ray diffractometer (Bruker, Germany), scanning electron microscope (ZEISS, Germany), transmission electron microscope (ZEISS, Germany), and X-ray photoelectron spectroscopy (Shimadzu, Japan), respectively. The surface charge and absorption peaks of the nanoparticles' functional groups were characterized using a zeta potential analyzer and UV–vis absorption spectroscopy (Agilent, USA), respectively.

PLA/GelMA scaffolds were prepared as reported in previous literature [53]. Briefly, 0.8 g of GelMA and 0.2 g of PLA were dissolved in 10 mL of hexafluoroisopropanol and formed into a homogeneous fibrous membrane using an electrostatic spinning machine. The fiber membrane was then broken down using a high-speed homogenizer. Gelatin/CeZnHAP microdroplets were prepared via a microfluidic device and crosslinked with 0.5 M EDC to form gelatin/CeZnHAP microspheres. The 0 °C pre-cooled microspheres and PLA/GelMA spun film suspension were then homogeneously mixed and transferred to −80 °C molds for rapid prototyping, lyophilization, and cross-linking under UV light for 5 min using the pre-cooled LAP solution to obtain the scaffolds. The appearance and mechanical stability of the scaffolds were recorded using a digital camera, while the morphology of the gelatin microspheres was observed using an optical microscope and analyzed for particle size distribution using Image J software. The structures of the composite scaffolds and their individual components were analyzed using Fourier-transform infrared spectroscopy (Thermo, USA). The degradation rate of gelatin/CeZnHAP microspheres within the PLA/GelMA scaffolds was assessed in PBS solution at 37 °C.

Cell viability of mitochondrial rheostats: Macrophages were Raw264.7 cell line. BMSC cells were extracted according to previous literature [54]. Briefly, femurs and tibiae were surgically isolated from 80 g SD rats, and their medullary cavities were flushed to obtain bone marrow suspensions. The suspensions were then diluted with α-MEM (HyClone, USA) medium supplemented with 10 % FBS and 1 % penicillin/streptomycin and cultured in 25 cm^2 cell culture flasks, with the medium changed every two days. BMSCs used in the experiments were from passages 3 to 6. Scaffolds were prepared using DMEM (HyClone, USA) and α-MEM extracts supplemented with 10 % serum. These

extracts were co-cultured with Raw264.7 cells and BMSCs in 96-well plates, with the medium changed every two days. Cell viability was assessed on days 1, 3, and 5 using the CCK-8 kit (Beyotime, China). On the third day, cytoskeleton staining was performed on Raw264.7 cells and BMSCs, and images were captured using fluorescence microscopy (Nikon, Japan).

Mitochondrial targeting of mitochondrial rheostats: To verify the mitochondrial targeting of CeZnHAP, we labeled the surface of CeZnHAP nanoparticles with FITC (Solarbio, China) and co-incubated them with Raw264.7 cells for 12 h. The FITC-labeled CeZnHAP nanoparticles and mitochondria of macrophages, labeled with mitochondrial probes, were observed using laser confocal microscopy (ZEISS, Germany). Additionally, changes in the membrane potential of macrophage mitochondria after treatment with different materials were detected using the JC-1 kit (Beyotime, China). The ROS levels generated by macrophage mitochondria were assessed using a DCFH-DA and MitoSOX Red fluorescent probe (Beyotime, China). Flow cytometry was used to detect ROS-expressing macrophages, a SOD activity assay kit was used to detect superoxide dismutase activity within macrophages, and the NF-κB p65 pathway was validated by western blots using anti-NF-κB p65 (ab32536, abcam) and anti-phosphor-NF-κB p65 antibodies (ab76302, abcam).

Mitochondrial metabolism targeting of mitochondrial rheostats: Macrophages were immobilized to assess the status of mitochondria by SEM (ZEISS, Germany). Liquid chromatography-tandem mass spectrometry (LC-MS/MS, Agilent, America) was used in metabolomics to evaluate the glucose metabolites of macrophages. Seahorse XFe96 (Agilent, America) was used to detect energy metabolism in macrophages. The level of oxidative phosphorylation in macrophages was assessed by injecting oligomycin (Oligo), carbonyl cyanide p-trifluoromethoxyphenylhydrazone (FCCP), and rotenone to measure the real-time oxygen consumption rate (OCR) of macrophages. Simultaneously, real-time extracellular acidification rates (ECARs) were measured by injecting glucose, oligomycin (Oligo), and 2-deoxy-D-glucose (2-DG) to assess glycolytic metabolic capacity.

Immunofluorescence staining of macrophages after mitochondrial rheostats treatment: macrophage-specific markers (CD86 and CD206) were stained and recorded by laser confocal microscopy. Briefly, cells were fixed with paraformaldehyde solution for 15 min, followed by permeabilization with 0.2 % Triton X-100 for 10 min, and then blocked with same-host serum for 1 h. Macrophages were subsequently treated with CD86 antibody (Abcam, 1:1000) and CD206 antibody (Abcam, 1:1000) for 12 h. Actin-Tracker Red-555 (Beyotime, China) and DAPI (Beyotime, China) were used to stain the cytoskeleton and nucleus, respectively. The fluorescence intensity of CD86 and CD206 was analyzed using ImageJ software.

The supernatant was collected after macrophages were co-cultured with the scaffold, and the levels of TNF-α and IL-10 secreted by macrophages were quantitatively measured using an ELISA kit (Beyotime, China). Subsequently, the cells were collected, and the ratio of inflammatory to anti-inflammatory macrophages was analyzed using flow cytometry. Real-time quantitative PCR was performed to detect the expression of macrophage-related genes, including IL-1β, INOS, Arg-1, IL-10, HK2, GLUT, and PKM2.

In vitro immuno-osteogenic differentiation properties of mitochondrial rheostats: to assess the osteogenic differentiation ability of the scaffolds, conditioned medium after co-incubation of the scaffolds with macrophages (containing 100 nM dexamethasone (Solarbio, China), 50 μM ascorbic acid (Solarbio, China) and 10 mM sodium β-glycerophosphate (Solarbio, China)) were used to culture BMSCs for alkaline phosphatase staining (Beyotime, China) and alizarin red staining (Solarbio, China) at 7 and 21 days, respectively. Osteogenic markers of BMSCs (OCN and COL-I) were stained and recorded by laser confocal microscopy. Briefly, cells were fixed for 15 min by paraformaldehyde solution, followed by permeabilization of cells by 0.2 % Triton X-100 for 10 min and blocked with same-host serum for 1 h. BMSCs were then treated with antibodies against OCN (Abcam, 1:1000) and COL-I (Abcam, 1:1000) for 12 h. Actin-tracker red-555 and DAPI were used to stain the cytoskeleton and nucleus. The fluorescence intensity of OCN and COL-I was detected by Image J. Real-time fluorescence quantitative PCR (Thermo, America) to detect the expression of macrophage-related genes (ALP, RUNX2, COL-I, OPN, and OCN).

Animal experiments: femoral defects and scaffold implantation: A rat femoral condylar defect model was established to de-evaluate the role of scaffolds in the early immune microenvironment and late osteogenesis. All animal experiments were approved by the Animal Ethics Committee of Ruijin Hospital, Shanghai Jiaotong University (Ethics No. 2023-03-SGKYJS-CWG-043). 40 male SD rats (280–320 g) were used in the study, and the experiments were divided into 5 groups ($n = 8$): (1) control group; (2) FM group; (3) HAP group; (4) ZnHAP group; (5) CeZnHAP group. Animals were anesthetized with isoflurane gas in the experiment. A defect with a diameter of 3 mm and a depth of 4 mm was created at the femoral condyle site using a medical kirschner needle, and the scaffold was subsequently implanted into the defect site. The rats were administered antibiotics daily for 3 days post-surgery and monitored for survival. The rats were euthanized by overdose anesthesia at 1, 2, and 4 weeks, respectively.

Micro-CT assessment of bone regeneration: Imaging evaluations were conducted *in vivo* to quantitatively and qualitatively compare bone regeneration indices following scaffold implantation. The bone quality of rats sampled at 2 and 4 weeks was assessed using a Micro-CT scanner (SkyScan 1276, Germany), and three-dimensional reconstructed images of bone tissue were generated using Mimics software. Bone trabecular volume fraction (BV/TV), bone mineral density (BMD), trabecular separation (Tb.Sp), and trabecular thickness (Tb.Th) were analyzed to assess the bone regeneration status.

Histological evaluation: Histological evaluations were conducted *in vivo* to quantitatively and qualitatively compare bone regeneration indices following scaffold implantation. Femoral condyle samples were collected from rats at 1, 2, and 4 weeks, fixed in 4 % paraformaldehyde for 48 h, decalcified for 4 weeks, and embedded in paraffin. The status of new bone formation at the defect sites was assessed using hematoxylin-eosin (HE) staining and Masson's trichrome staining (Masson). Additionally, the expression levels of CD206, INOS, and OPN in the tissues were analyzed by immunofluorescence staining and quantified using ImageJ software. *Statistical analysis:* The experiment was repeated at least three times, and the results were expressed as mean ± standard deviation. GraphPad Prism 9.0 and Origin 2018 software were used for plotting and statistical analysis. student-t test and ANOVA were employed to compare experimental data (ns, no significant difference, $^{*}p < 0.05$, $^{**}p < 0.005$, $^{***}p < 0.001$, $^{****}p < 0.0001$).

CRediT authorship contribution statement

Pengzhen Zhuang: Writing – original draft, Software, Methodology, Investigation, Data curation. **Yu Chen:** Writing – original draft, Investigation, Data curation. **Yu Zhang:** Writing – original draft, Software, Data curation. **Wu Yang:** Writing – original draft, Investigation, Data curation. **Guilai Zuo:** Writing – original draft, Investigation, Data curation. **Jessica M. Rosenholm:** Writing – review & editing, Methodology. **Zhongmin Wang:** Writing – review & editing, Methodology. **Juan Wang:** Writing – review & editing, Methodology, Investigation, Data curation. **Wenguo Cui:** Writing – review & editing, Supervision, Methodology, Investigation. **Hongbo Zhang:** Writing – review & editing, Supervision, Software, Methodology, Investigation.

Data availability

Data will be made available on request.

Ethics approval and consent to participate

All animal experiments were approved by the Animal Ethics

Committee of Ruijin Hospital, Shanghai Jiaotong University (Ethics No. 2023-03-SGKYJS-CWG-043). All the authors were in compliance with all relevant ethical regulations.

Declaration of competing interest

Hongbo Zhang is an editorial board member for Bioactive Materials and was not involved in the editorial review or the decision to publish this article. The authors declare that they have no known competing financial interests or personal relationships that could have appeared to influence the work reported in this paper.

Acknowledgement

Pengzhen Zhuang and Yu Chen contributed equally to this work. This work was supported by the Program of Shanghai Academic/Technology Research Leader (22XD1422600), the Research Fellow (Grant No.353146), Research Project (347897), Solution for Health Profile (336355), InFLAMES Flagship (337531) grants and Printed Intelligence Infrastructure" (PII-FIRI) from Research Council of Finland. This study is part of the activities of the Åbo Akademi University Foundation (SÅA) funded Center of Excellence in Research "Materials-driven solutions for combating antimicrobial resistance (MADNESS)" at ÅAU.

Appendix A. Supplementary data

Supplementary data to this article can be found online at https://doi.org/10.1016/j.bioactmat.2025.03.008.

References

[1] J. Ma, K. Wei, J. Liu, K. Tang, H. Zhang, L. Zhu, J. Chen, F. Li, P. Xu, J. Chen, J. Liu, H. Fang, L. Tang, D. Wang, L. Zeng, W. Sun, J. Xie, Y. Liu, B. Huang, Glycogen metabolism regulates macrophage-mediated acute inflammatory responses, Nat. Commun. 11 (2020) 1769.

[2] L. Ma, W. Li, Y. Zhang, L. Qi, Q. Zhao, N. Li, Y. Lu, L. Zhang, F. Zhou, Y. Wu, Y. He, H. Yu, Y. He, B. Wei, H. Wang, FLT4/VEGFR3 activates AMPK to coordinate glycometabolic reprogramming with autophagy and inflammasome activation for bacterial elimination, Autophagy 18 (6) (2021) 1385–1400.

[3] S.K. Wculek, I. Heras-Murillo, A. Mastrangelo, D. Mañanes, M. Galán, V. Miguel, A. Curtabbi, C. Barbas, N.S. Chandel, J.A. Enríquez, S. Lamas, D. Sancho, Oxidative phosphorylation selectively orchestrates tissue macrophage homeostasis, Immunity 56 (3) (2023) 516–530.

[4] F. Wang, S. Zhang, I. Vuckovic, R. Jeon, A. Lerman, C.D. Folmes, P.P. Dzeja, J. Herrmann, Glycolytic stimulation is not a requirement for M2 macrophage differentiation, Cell Metab. 28 (3) (2018) 463–475.

[5] S. Xu, K.Q. Deng, C. Lu, X. Fu, Q. Zhu, S. Wan, L. Zhang, Y. Huang, L. Nie, H. Cai, Q. Wang, H. Zeng, Y. Zhang, F. Wang, H. Ren, Y. Chen, H. Yan, K. Xu, L. Zhou, M. Lu, Y. Zhu, S. Liu, Z. Lu, Interleukin-6 classic and trans-signaling utilize glucose metabolism reprogramming to achieve anti- or pro-inflammatory effects, Metabolism 155 (2024) 155832.

[6] H. Wu, X. Zhao, S.M. Hochrein, M. Eckstein, G.F. Gubert, K. Knopper, A. M. Mansilla, A. Oner, R. Doucet-Ladeveze, W. Schmitz, B. Ghesquiere, S. Theurich, J. Dudek, G. Gasteiger, A. Zernecke, S. Kobold, W. Kastenmuller, M. Vaeth, Mitochondrial dysfunction promotes the transition of precursor to terminally exhausted T cells through HIF-1α-mediated glycolytic reprogramming, Nat. Commun. 14 (2023) 6858.

[7] Y. Tang, J. Zhu, D. Huang, X. Hu, Y. Cai, X. Song, Z. Song, C. Hong, Z. Feng, F. Kang, Mandibular osteotomy-induced hypoxia enhances osteoclast activation and acid secretion by increasing glycolysis, J. Cell. Physiol. 234 (7) (2019) 11165–11175.

[8] Y. Wang, N. Li, X. Zhang, T. Horng, Mitochondrial metabolism regulates macrophage biology, J. Biol. Chem. 297 (1) (2021) 100904.

[9] Y. Mi, M. Tang, Q. Wu, Y. Wang, Q. Liu, P. Zhu, X. Xue, Y. Liu, X. Chai, Y. Hou, D. Yan, NMAAP1 regulated macrophage polarizion into M1 type through glycolysis stimulated with BCG, Int. Immunopharmacol. 126 (5) (2024) 111257.

[10] F.J. Weisel, S.J. Mullett, R.A. Elsner, A.V. Menk, N. Trivedi, W. Luo, D. Wikenheiser, W.F. Hawse, M. Chikina, S. Smita, L.J. Conter, S.M. Joachim, S. G. Wendell, M.J. Jurczak, T.H. Winkler, G.M. Delgoffe, M.J. Shlomchik, Germinal center B cells selectively oxidize fatty acids for energy while conducting minimal glycolysis, Nat. Immunol. 21 (2020) 331–342.

[11] L. Ye, Y. Jiang, M. Zhang, Crosstalk between glucose metabolism, lactate production and immune response modulation, Cytokine Growth Factor Rev. 68 (2022) 81–92.

[12] S. Willenborg, D.E. Sanin, A. Jais, X. Ding, T. Ulas, J. Nüchel, M. Popović, T. MacVicar, T. Langer, J.L. Schultze, A. Gerbaulet, A. Roers, E.J. Pearce, J. C. Brüning, A. Trifunovic, S.A. Eming, Mitochondrial metabolism coordinates stage-specific repair processes in macrophages during wound healing, Cell Metab. 33 (12) (2021) 2398–2414.

[13] K. Wu, X. Xu, M. Wu, X. Li, M. Hoque, G. Li, Q.u Lian, K. Long, T. Zhou, H. Piao, A. Xu, H. Hui, K. Cheng, MDM2 induces pro-inflammatory and glycolytic responses in M1 macrophages by integrating iNOS-nitric oxide and HIF-1α pathways in mice, Nat. Commun. 15 (2024) 8624.

[14] Y. Wang, E. Stancliffe, R. Fowle-Grider, R. Wang, C. Wang, M. Schwaiger-Haber, L. P. Shriver, G.J. Patti, Saturation of the mitochondrial NADH shuttles drives aerobic glycolysis in proliferating cells, Mol. Cell 82 (17) (2022) 3270–3283.

[15] J. Sim, A.S. Cowburn, A. Palazon, B. Madhu, P.A. Tyrakis, D. Macías, D. M. Bargiela, S. Pietsch, M. Gralla, C.E. Evans, T. Kittipassorn, Y.C.J. Chey, C. M. Branco, H. Rundqvist, D.J. Peet, R.S. Johnson, The factor inhibiting HIF asparaginyl hydroxylase regulates oxidative metabolism and accelerates metabolic adaptation to hypoxia, Cell Metab. 27 (4) (2018) 898–913.

[16] R. Lan, Y. Zhou, Z. Wang, S. Fu, Y. Gao, X. Gao, J. Zhang, X. Han, V. Phouthapane, Y. Xu, J. Miao, Reduction of ROS-HIF1α-driven glycolysis by taurine alleviates Streptococcus uberis infection, Food Funct. 13 (2022) 1774–1784.

[17] A. Patgiri, O.S. Skinner, Y. Miyazaki, G. Schleifer, E. Marutani, H. Shah, R. Sharma, R.P. Goodman, T.L. To, X. Robert Bao, F. Ichinose, W.M. Zapol, V.K. Mootha, An engineered enzyme that targets circulating lactate to alleviate intracellular NADH: NAD+ imbalance, Nat. Biotechnol. 38 (2020) 309–313.

[18] L. Ran, S. Zhang, G. Wang, P. Zhao, J. Sun, J. Zhou, H. Gan, R. Jeon, Q. Li, J. Herrmann, F. Wang, Mitochondrial pyruvate carrier-mediated metabolism is dispensable for the classical activation of macrophages, Nat. Metab. 5 (2023) 804–820.

[19] P.L. Graney, S. Ben-Shaul, S. Landau, A. Bajpai, B. Singh, J. Eager, A. Cohen, S. Levenberg, K.L. Spiller, Macrophages of diverse phenotypes drive vascularization of engineered tissues, Sci. Adv. 6 (18) (2020) eaay6391.

[20] Y. Kuninaka, Y. Ishida, A. Ishigami, M. Nosaka, J. Matsuki, H. Yasuda, A. Kofuna, A. Kimura, F. Furukawa, T. Kondo, Macrophage polarity and wound age determination, Sci. Rep. 12 (2022) 20327.

[21] Y. Liu, R. Xu, H. Gu, E. Zhang, J. Qu, W. Cao, X. Huang, H. Yan, J. He, Z. Cai, Metabolic reprogramming in macrophage responses, Biomark. Res. 9 (2021) 1.

[22] J. Zhang, F. Huang, L. Chen, G. Li, W. Lei, J. Zhao, Y. Liao, Y. Li, C. Li, M. Chen, Sodium lactate accelerates M2 macrophage polarization and improves cardiac function after myocardial infarction in mice, Cardiovas. Ther. 2021 (2021) 5530541.

[23] H. Gu, Y. Zhu, J. Yang, R. Jiang, Y. Deng, A. Li, Y. Fang, Q. Wu, H. Tu, H. Chang, J. Wen, X. Jiang, Liver-inspired polyetherketoneketone scaffolds simulate regenerative signals and mobilize anti-inflammatory reserves to reprogram macrophage metabolism for boosted osteoporotic osseointegration, Adv. Sci. 10 (25) (2023) 2302136.

[24] X.T. He, X. Li, M. Zhang, B.M. Tian, L.J. Sun, C.S. Bi, D.K. Deng, H. Zhou, H.L. Qu, C. Wu, F.M. Chen, Role of molybdenum in material immunomodulation and periodontal wound healing: targeting immunometabolism and mitochondrial function for macrophage modulation, Biomaterials 283 (2022) 121439.

[25] G. Yang, J.S. Ni, Y. Li, M. Zha, Y. Tu, K. Li, Acceptor engineering for optimized ROS generation facilitates reprogramming macrophages to M1 phenotype in photodynamic immunotherapy, Angew. Chem. Int. Ed. 60 (10) (2021) 5386–5393.

[26] E.L. Mills, B. Kelly, A. Logan, A.S.H. Costa, M. Varma, C.E. Bryant, P. Tourlomousis, J.H.M. Däbritz, E. Gottlieb, I. Latorre, S.C. Corr, G. McManus, D. Ryan, H.T. Jacobs, M. Szibor, R.J. Xavier, T. Braun, C. Frezza, M.P. Murphy, L.A. O'Neill, Succinate dehydrogenase supports metabolic repurposing of mitochondria to drive inflammatory macrophages, Cell 167 (2) (2016) 457–470.

[27] B. Li, Y. Shi, M. Liu, F. Wu, X. Hu, F. Yu, C. Wang, L. Ye, Attenuates of NAD+ impair BMSC osteogenesis and fracture repair through OXPHOS, Stem Cell Res. Ther. 13 (2022) 77.

[28] C. Jorgensen, Maroun Khoury, M. Khoury, Musculoskeletal progenitor/stromal cell-derived mitochondria modulate cell differentiation and therapeutical function, Front. Immunol. 12 (2021) 606781.

[29] S. Wu, Y. Shi, L. Jiang, W. Bu, K. Zhang, W. Lin, C. Pan, Z. Xu, J. Du, H. Chen, H. Wang, N-Acetylcysteine-Derived carbon dots for free radical scavenging in intervertebral disc degeneration, Adv. Healthc. Mater. 12 (24) (2023) 2370144.

[30] M. Jiang, X. Li, J. Zhang, Y. Lu, Y. Shi, C. Zhu, Y. Liu, B. Qin, Z. Luo, Y. Du, L. Luo, L. Peng, J. You, Dual inhibition of endoplasmic reticulum stress and oxidation stress manipulates the polarization of macrophages under hypoxia to sensitize immunotherapy, ACS Nano 15 (9) (2021) 14522–14534.

[31] H. Wei, J. Qin, Q. Huang, Z. Jin, L. Zheng, J. Zhao, Z. Qin, Epigallocatechin-3-gallate (EGCG) based metal-polyphenol nanoformulations alleviates chondrocytes inflammation by modulating synovial macrophages polarization, Biomed. Pharmacother. 161 (2023) 114366.

[32] J. Ye, Q. Li, Y. Zhang, Q. Su, Z. Feng, P. Huang, C. Zhang, Y. Zhai, W. Wang, ROS scavenging and immunoregulative EGCG@Cerium complex loaded in antibacterial polyethylene glycol-chitosan hydrogel dressing for skin wound healing, Acta Biomater. 166 (2023) 155–166.

[33] X. Chen, L. Zhang, H. Zeng, W. Meng, G. Liu, W. Zhang, P. Zhao, Q. Zhang, M. Chen, J. Chen, Manganese-based immunomodulatory nanocomposite with catalase-like activity and microwave-enhanced ROS elimination ability for efficient rheumatoid arthritis therapy, Small 19 (50) (2023) 2304610.

[34] G. Huang, Y. Lin, L. Zhang, Z. Yan, Y. Wang, Y. Liu, Synthesis of sulfur-selenium doped carbon quantum dots for biological imaging and scavenging reactive oxygen species, Sci. Rep. 9 (2019) 19651.

[35] K.E. Martin, M.D. Hunckler, E. Chee, J.D. Caplin, G.F. Barber, P.P. Kalelkar, R. S. Schneider, A.J. García, Hydrolytic hydrogels tune mesenchymal stem cell persistence and immunomodulation for enhanced diabetic cutaneous wound healing, Biomaterials 301 (2023) 122256.

[36] M.M. Coronel, K.E. Martin, M.D. Hunckler, P. Kalelkar, R.M. Shah, A.J. García, Hydrolytically degradable microgels with tunable mechanical properties modulate the host immune response, Small 18 (36) (2022) 2106896.
[37] M.M. Carleton, M.V. Sefton, Injectable and degradable methacrylic acid hydrogel alters macrophage response in skeletal muscle, Biomaterials 223 (2019) 119477.
[38] J. Lin, D. Pan, Y. Sun, C. Ou, Y. Wang, J. Cao, The modification of gelatin films: based on various cross-linking mechanism of glutaraldehyde at acidic and alkaline conditions, Food Sci. Nutr. 7 (12) (2019) 4140–4146.
[39] J. Sapudom, M. Kongsema, A. Methachittipan, S. Damrongsakkul, S. Kanokpanont, J.C.M. Teo, M. Khongkow, K. Tonsomboon, P. Thongnuek, Degradation products of crosslinked silk fibroin scaffolds modulate the immune response but not cell toxicity, J. Mater. Chem. B 11 (2023) 3607–3616.
[40] M. Zheng, X. Wang, O. Yue, M. Hou, H. Zhang, S. Beyer, A.M. Blocki, Q. Wang, G. Gong, X. Liu, J. Guo, Skin-inspired gelatin-based flexible bio-electronic hydrogel for wound healing promotion and motion sensing, Biomaterials 276 (2021) 121026.
[41] F. Qin, H. Tan, Y. Yang, L. Xu, X. Yang, Upregulation of Cullin1 neddylation promotes glycolysis and M1 polarization of macrophage via NF-κB p65 pathway in sepsis, Funct. Integr. Genomics 24 (2024) 204.
[42] J. Liu, Y. Wei, W. Jia, C. Can, R. Wang, X. Yang, C. Gu, F. Liu, C. Ji, D. Ma, Chenodeoxycholic acid suppresses AML progression through promoting lipid peroxidation via ROS/p38 MAPK/DGAT1 pathway and inhibiting M2 macrophage polarization, Redox Biol. 56 (2022) 102452.
[43] Y. Zhong, Y. Yang, Y. Xu, B. Qian, S. Huang, Q. Long, Z. Qi, X. He, Y. Zhang, L. Li, W. Hai, X. Wang, Q. Zhao, X. Ye, Design of a Zn-based nanozyme injectable multifunctional hydrogel with ROS scavenging activity for myocardial infarction therapy, Acta Biomater. 177 (2024) 62–76.
[44] F. Ye, L. Wu, H. Li, X. Peng, Y. Xu, W. Li, Y. Wei, F. Chen, J. Zhang, Q. Liu, SIRT1/PGC-1α is involved in arsenic-induced male reproductive damage through mitochondrial dysfunction, which is blocked by the antioxidative effect of zinc, Environ. Pollut. 320 (2023) 121084.
[45] A. Lao, J. Wu, D. Li, A. Shen, Y. Li, Y. Zhuang, K. Lin, J. Wu, J. Liu, Functionalized metal–organic framework-modified hydrogel that breaks the vicious cycle of inflammation and ROS for repairing of diabetic bone defects, Small 19 (36) (2023) 2206919.
[46] M. Soh, D.W. Kang, H.G. Jeong, D. Kim, D.Y. Kim, W. Yang, C. Song, S. Baik, I. Y. Choi, S.K. Ki, H.J. Kwon, T. Kim, C.K. Kim, S.H. Lee, T. Hyeon, Ceria–zirconia nanoparticles as an enhanced multi-antioxidant for sepsis treatment, Angew. Chem. Int. Ed. 129 (38) (2017) 11557–11561.
[47] X. Gao, B. Wang, J. Li, B. Niu, L. Cao, X.j. Liang, J. Zhang, Y. Jin, X. Yang, Catalytic tunable black phosphorus/ceria nanozyme: a versatile oxidation cycle accelerator for alleviating cisplatin-induced acute kidney injury, Adv. Healthc. Mater. 12 (30) (2023) 2301691.
[48] J. Yan, Y. Wang, Z. Mu, X. Han, L. Bi, X. Wang, P. Song, Y. Kang, L. Wang, X. Zhang, Y. Wang, H. Zhang, Gold nanobipyramid-mediated apoptotic camouflage of adipocytes for obesity immunotherapy, Adv. Mater. 35 (8) (2022) 2207686.
[49] Q.-X. Huang, J.-L. Liang, Q.-W. Chen, X.-K. Jin, M.-T. Niu, C.-Y. Dong, X.-Z. Zhang, Metal-organic framework nanoagent induces cuproptosis for effective immunotherapy of malignant glioblastoma, Nano Today 51 (2023) 101911.
[50] B. Yang, H. Yao, J. Yang, C. Chen, Y. Guo, H. Fu, J. Shi, In situ synthesis of natural antioxidase mimics for catalytic anti-inflammatory treatments: rheumatoid arthritis as an example, J. Am. Chem. Soc. 144 (1) (2021) 314–330.
[51] X. Fu, Y. Li, T. Huang, Z. Yu, K. Ma, M. Yang, Q. Liu, H. Pan, H. Wang, J. Wang, M. Guan, Runx2/Osterix and zinc uptake synergize to orchestrate osteogenic differentiation and citrate containing bone apatite formation, Adv. Sci. 5 (4) (2018) 1700755.
[52] Y. Mao, Y. Chen, W. Li, Y. Wang, J. Qiu, Y. Fu, J. Guan, P. Zhou, Physiology-inspired multilayer nanofibrous membranes modulating endogenous stem cell recruitment and osteo-differentiation for staged bone regeneration, Adv. Healthc. Mater. 11 (21) (2022) 2201457.
[53] P. Tang, P. Song, Z. Peng, B. Zhang, X. Gui, Y. Wang, X. Liao, Z. Chen, Z. Zhang, Y. Fan, Z. Li, Y. Cen, C. Zhou, Chondrocyte-laden GelMA hydrogel combined with 3D printed PLA scaffolds for auricle regeneration, Mat. Sci. Eng. C-Mater. 130 (2021) 112423.
[54] P. Zhuang, X. Wu, H. Dai, Y. Yao, T. Qiu, Y. Han, S. Li, Nano β-tricalcium phosphate/hydrogel encapsulated scaffolds promote osteogenic differentiation of bone marrow stromal cells through ATP metabolism, Mater. Des. 208 (2021) 109881.